Vessel distance mapping reveals mesoscopic arterial and venous patterns in the putamen

Hendrik Mattern[1,2,3*], Berta Garcia-Garcia[2], Stefanie Böwe[4], Grazia Mietzner[4], Solveig Henneicke[2,4], Oliver Speck[1,2,4,5], Stefanie Schreiber[2,3,4]

1 Biomedical Magnetic Resonance, Otto-von-Guericke-University Magdeburg, 39120 Magdeburg, Germany

2 German Center for Neurodegenerative Diseases, 39120 Magdeburg, Germany

3 Center for Behavioral Brain Sciences (CBBS), 39106 Magdeburg, Germany

4 Department of Neurology, Otto-von-Guericke University, Magdeburg, Germany

5 Leibniz Institute for Neurobiology, 39118 Magdeburg, Germany

* corresponding author: Dr.-Ing. Hendrik Mattern; Leipziger Str. 44, 39120 Magdeburg, Germany, H65-395; +49 391 67-56118; hendrik.mattern@ovgu.de

Abstract

Purpose:

While vessel atlases, i.e. building one global mean representative vascular model, and vessel patterns, i.e. finding distinct differences in how a structure is vascularized across subjects, have gained momentum recently, both concepts are treated as two separated entities currently. The aim of this study was to bridge vessel atlases and patterns by identifying distinct arterial and venous vascular patterns in the human putamen at the mesoscopic scale using MRI.

Methods:

High resolution MRI of 20 healthy subjects (40 hemispheres) is leveraged to compute arterial and venous segmentations, respectively. The recently introduced Vessel Distance Mapping (VDM) framework was combined with so-called vascular fingerprints to find arterial and venous patterns in an unsupervised manner, respectively. As a complementary approach, qualitative pattern descriptions and expert ratings were generated. The patterns found are compared with each other and to the global mean in native image space and after spatial normalization to MNI space, respectively.

Results:

Automatic clustering and expert rating found similar vessel patterns in the putamen, with arterial and venous patterns following a unimodal and bimodal distribution, respectively. When neglecting patterns with single putamen assigned, the automatic clustering found 4 arterial and 3 venous, while the expert rating found 3 arterial and 4 venous patterns. While the patterns showed distinct differences w.r.t. each

other, arterial vascularization in the putamen is well described by one global mean with unimodal distributed subject-specific variations. Venous pattern showed a bimodal distribution with either a lower or higher vascularization then the global mean, limiting the representative character of a single global representation as commonly used in vessel atlases.

Conclusion:

To you best knowledge, this is the first description of distinctively different vessel patterns in the human putamen using MRI. Further, we provide tools to investigate the vasculature beyond global averages, i.e. by identifying vessel patterns using either unsupervised clustering or expert ratings. Furture applications included assessment of vessel biases in layer-specific function MRI and vascular resistance and resilience mechanisms in pathologies. Overall, the study advocates the use of vessel pattern-specifics atlases which become more relevant with increasing imaging resolutions as vessel patterns become more heterogeneous and explicit vessel co-registration is no longer possible.

Key words: Vessel distance mapping; magnetic resonance imaging; ultra-high field; vessel imaging; vasculature;

Introduction

The vasculature has a profound effect on the brain's function in health and disease. In recent years, tremendous progress with respect to mapping the vasculature has been made, such as the introduction of magnetic resonance imaging (MRI)-based vessel atlases (Huck et al. 2019; Bernier et al. 2018; Ward et al. 2018; Viviani 2016; Grabner et al. 2014; Mouches and Forkert 2019; Forkert et al. 2013; Dufour et al. 2013). The main objective of these atlases was to provide the methodology to map and quantify the vasculature (similar to voxel-based morphometry (Ashburner and Friston 2000)). Further, understanding the vascular bias of the functional MRI (fMRI) signal was a driving force for these atlases.

Besides these neuroscientific incentives to map the vasculature *in vivo*, neurological studies investigated vessel patterns as mechanisms for resistance and resilience towards pathologies. The hippocampal arterial vessel pattern, i.e. whether or not the anterior choroidal artery is involved in the supply of the hippocampus, has been linked to cognitive reserve in cerebral small vessel disease (Perosa et al. 2020; Vockert et al. 2021).

This study aims to close the gap between the neuroscientific and neurological approach, hence, bring vessel mapping and vessel pattern into one framework. In this proof-of-principle study, the arterial and venous vasculature in the human putamen are studied at the mesoscopic scale (defined in this study as voxel volumes of approx. 0.125 mm^3 or less). To that end, high resolution MRI is used and the following ideas as well as challenges are addressed:

1) While explicit vessel co-registration, i.e. matching the positions of vessels across subjects, is a powerful tool to normalize the cerebral vascular tree, the vasculature becomes more variable across subjects with decreasing vessel diameter (Huck et al. 2019; Bernier et al. 2018). When leveraging high resolution MRI

to assess the vasculature at the mesoscopic scale, inter-subject vessel probabilities decrease with decreasing vessel diameter even when using vessel co-registration (Bernier et al. 2018). This is due to inter-subject variabilities of higher order branches of the vascular tree, i.e. different number of arteries supplying the putamen across subjects (Akashi et al. 2012; Wei et al. 2022). Instead of enforcing one-on-one matches of the vasculature across subjects, we propose to perform only spatial normalization and using vessel distance maps instead of vessel overlaps or densities. This is motivated by past studies leveraging vessel distances (Huck et al. 2019; Bernier et al. 2018; Bause et al. 2020; Haast et al. 2021) and further extended for pattern assessment in this study. We coined the approach Vessel Distance Mapping (VDM) (Garcia-Garcia et al. 2023) and envisioned VDM as complementary approach to vessel densities (Feldman et al. 2020).

2) Beyond vessel atlas building, a framework is proposed to find distinct vessel patterns in the putamen i.e. identify differences in how the vessels propagate through a region of interest. To that end, expert rating as well as a complementary automatic approach using clustering of so-called vascular fingerprints is proposed. The main incentive is to test if distinct vessel patterns in the putamen exist and how well these would be represented by a single average vessel atlas.

To test the proposed methodology the putamen was selected for four reasons. First and as mentioned before, its vasculature is highly variable across subjects, rendering vessel co-registrations arguably infeasible. Second, Huck et al. excluded all deep gray matter in their high-resolution venous atlas (Huck et al. 2019), rendering an assessment of the putamen's venous vasculature valuable. Fourth, the putamen's arteries supply neurologically critical zones (Takahashi 2010). Last, the putamen and its vasculature can be depicted reliably using high-resolution MRI (Mattern et al. 2018; Mattern et al. 2019; Akashi et al. 2012; Conijn et al. 2009; Kang et al. 2009; Ward et al. 2018; Huck et al. 2019; Bernier et al. 2018) and, therefore, enable the proposed vessel pattern assessment at the mesoscopic scale.

Methods

In the following the data used, image processing applied, methods implemented, and statistical assessment performed are explained. The aim was to identify distinctively different arterial and venous patterns in the human putamen. To avoid ambiguity, vessel patterns are defined in this study as how the vessels propagate through the brain as well as their distances and organization with respect to each other. Although highly relevant from a neurological perspective, within this study, a vessel pattern does not refer to the origin of supply or drainage.

Data

The publicly available "StudyForrest" dataset was re-used in this study (https://www.studyforrest.org/data.html) (Hanke et al. 2014). Although originally intended to study the human brain's function, the dataset includes structural data to study the arterial and venous vasculature. Twenty right-handed participants (age 21–38 years, mean age 26.6 years, 12 males; gave written consent; study approved by local ethics committee) were included (Hanke et al. 2014).

Subjects were scanned at 3-Tesla (3T) to obtain T1-weighted and T2*-weighted data as well as at 7-Tesla (7T) to acquire Time-of-Flight (ToF) angiography. At 3T (Philips Achieva equipped with a 32 channel head

coil), a whole brain T1-weighted Turbo Field Echo sequence with 0.7 mm isotropic resolution (repetition time (TR)/ inversion time (TI)/ echo time (T)E = 2500/900/5.7 ms) and a T2*-weighted, 3D PRESTO fast field echo sequence with 0.43x0.43x0.7 (reconstructed to 0.35) mm; (500 axial slices, with TR/shifted TE = 19/26ms) were acquired (Liu et al. 1993; Hanke et al. 2014).

At 7T (Siemens 7 T Classic, Siemens Healthineers, Erlangen, Germany) equipped with a 32 channel Nova Medical Inc, MA, USA), a MOTSA ToF angiography was acquired with four slabs each 52 slices, and 0.3x0.3x0.3mm voxel size (Parker et al. 1991; Hanke et al. 2014).

Registration to MNI space

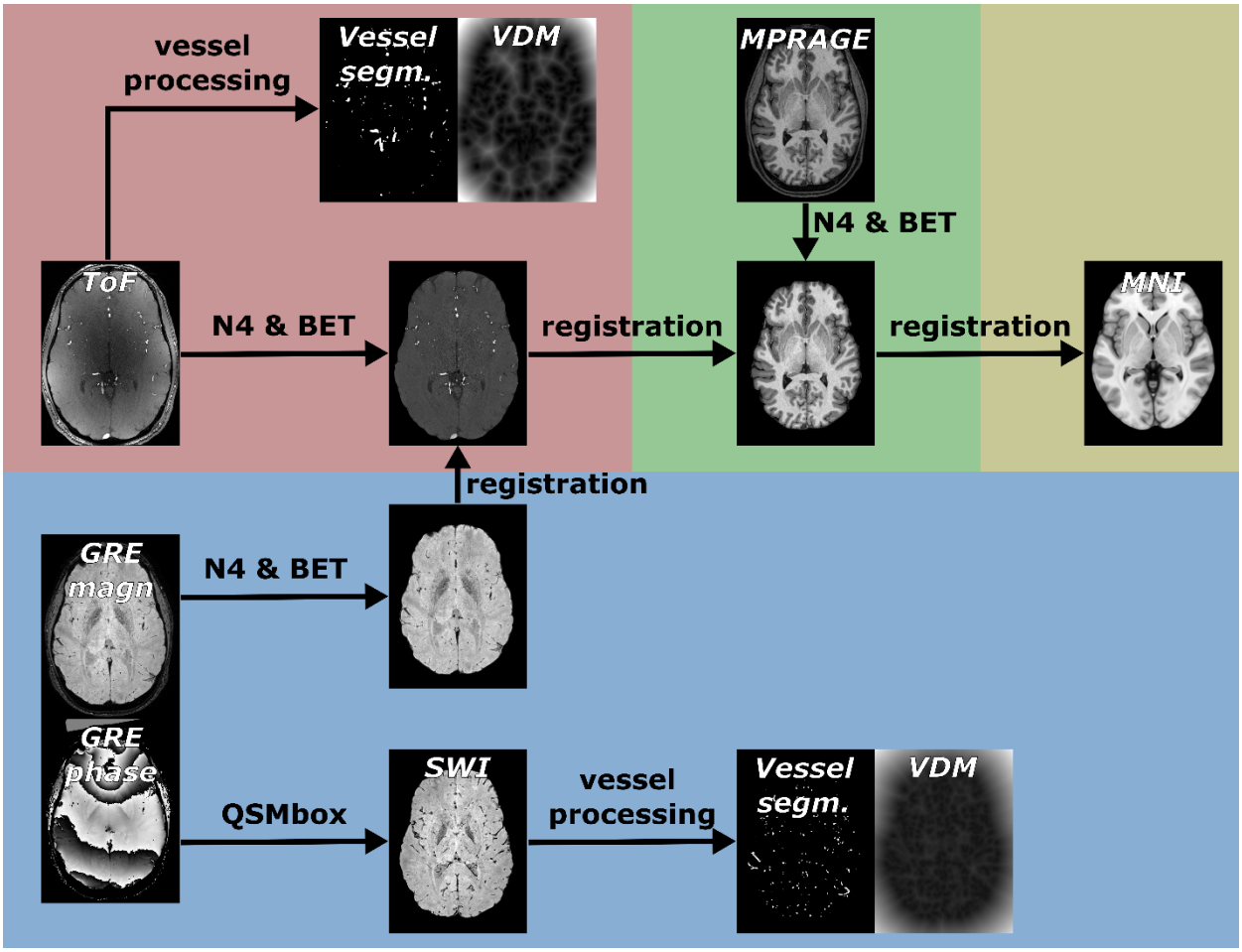

Figure 1: Image processing pipeline showing how the data is processed and registered to transform it from the subject-specific native image space into the MNI space for group analysis. Registration is done using the bias-field corrected and brain-extracted magnitude images (done with N4 & BET). Vessel segmentation and vessel distance mapping (VDM) is performed in the native space, respectively, and transformed subsequently to the MNI space using the transforms found for the magnitude images. Each space is color-coded: blue – subject-specific GRE space; red – subject-specific ToF space; green – subject-specific T1-weighed (T1-w) space; yellow – MNI space for group analysis.

Figure 1 shows all processing and co-registration steps performed. Prior to co-registration all T1-weighted, magnitude images of the T2*-weighted and ToF volumes were bias field corrected using N4BiasFieldCorrection (Tustison et al. 2010) provided by ANTs (Avants et al. 2011) and subsequently skull-

stripped using BET2 provided by FSL (lenient fractional threshold of 0.1 and brain center estimation enabled; small field-of-view (FOV) option enabled for ToF angiography) (Smith 2002).

After processing, but prior to co-registration, a left-right flipped copy of the data was generated per subject to enable voxel-by-voxel comparisons across hemispheres in the MNI space (asymmetric versions of MNI template and atlas were used). Hence, per subject, two datasets (original and mirrored version) existed and where co-registered individually. Per dataset, the 3T, T2*-weighted magnitude images were registered affinely to the corresponding 7T ToF volume. Subsequently, the ToF images were registered affinely to the subject's T1-weighted data. Finally, the T1-weighted data were registered non-linearly (symmetric diffeomorphic image (Avants et al. 2008)) to the MNI template (mni_icbm152_t1_tal_nlin_asym_09b_hires from http://nist.mni.mcgill.ca/icbm-152-nonlinear-atlases-2009/, 0.5mm isotropic resolution). All registrations were performed with ANTs (Avants et al. 2011; Avants et al. 2008). Using the output of the registrations, the vessel distance maps of all subjects were transformed into the MNI space to enable voxel-wise comparisons and generate a global group average.

To identify the putamen, the Harvard-Oxford subcortical atlas (asymmetric version) was used (Makris et al. 2006; Frazier et al. 2005; Goldstein et al. 2007; Desikan et al. 2006). To bring the masks into the native image space, the inverses of the registration transforms were used per subject. Individual masks for left and right putamen where used when working in subject space. When working in MNI space, only the left putamen mask of the MNI template was used as a dedicated co-registration to the asymmetric MNI template for the original and left-right mirrored data existed per subject i.e. left and right putamen in subject space where co-registered to the left putamen in MNI space.

Computation of susceptibility weighted images

To enhance the venous vasculature, susceptibility weighted images (SWI) were generated from the unprocessed T2*-weighted magnitude and phase data. SWI were generated using high-pass filtered quantitative susceptibility mapping (QSM) since QSM-based SWI showed qualitatively sharper images than conventional SWI (Acosta-Cabronero et al. 2018). In brief, QSM-based SWI reconstruction were generated with QSMbox (Acosta-Cabronero et al. 2018) (available at https://gitlab.com/acostaj/QSMbox/-/tree/master) by performing the following steps:

First, a brain mask is determined for the magnitude volume with BET2 (Smith 2002). Subsequently, the phase data were unwrapped using a discrete Laplacian method (Schofield and Zhu 2003) (MEDI toolbox implementation) followed by background field removal using Laplacian boundary value filtering (Zhou et al. 2014) (available from MEDI toolbox). To suppress local field inductions from large structures, high-pass filtered field maps were generated with the variable spherical mean filtering approach (Bilgic et al. 2016; Schweser et al. 2011; Li et al. 2011) using a starting radius of 3 mm. Using small radii suppresses low spatial frequencies, hence, only small structures such as the vasculature are enhanced in the final susceptibility maps (Acosta-Cabronero et al. 2018; Mattern et al. 2019). To generate these maps, the multi-scale dipole inversion (MSDI) (Acosta-Cabronero et al. 2018) was applied to the high-pass filtered field map. To further enhance small susceptibility sources such as veins, an additional high-pass was applied. Conventionally, MSDI uses a Laplacian-pyramid to compute the QSM by iterating from the finest to the coarsest spatial scale. Here, only the first scale (spherical mean value radius = 1mm) was used to suppress large structures further. Finally, the high-pass filtered QSM was used to generate QSM-based SWI following Acosta-

Cabronero et al. (Acosta-Cabronero et al. 2018): First, voxel-wise weights W are computed by rescaling the susceptibility values χ from 0 to 1 using a cut-off value c of 0.2 ppm

$$W = \begin{cases} 0, & \text{for } \chi > c \\ \dfrac{c - \chi}{c}, & \text{for } 0 \leq \chi \leq c \\ 1, & \text{otherwise} \end{cases}$$

Second, the weights W are raised to the power four and multiplied with the T2*-weighted magnitude images to yield the final QSM-based SWI images. Hence, the hypointense voxels in the magnitude images are further suppressed if their susceptibility is high (i.e. indicating iron-rich structures such as vessels).

Note that although the described high-pass filtering suppresses large structure, non-venous, iron-rich structure on the scale of the vasculature are not suppressed. Suppressing for non-venous contribution is further described in the following vessel enhancement and segmentation section.

Vessel enhancement and segmentation

Arteries and veins were segmented from ToF angiography and QSM-based SWI in their respective native space using a Frangi vesselness filter (Frangi et al. 1998) and subsequent hysteresis thresholding (Fraz et al. 2011). The segmentation is based on the Openly available sMall vEsseL sEgmenTa-Tion pipeline (Mattern 2021a) (available at https://gitlab.com/hmattern/omelette). First, a top-hat preprocessing was performed to eliminate large structures from the image using morphological operations prior to vessel enhancement. Subsequently, the Frangi filter enhances tubular structures by computing the Hessian of the image and analyzing the ratio and sign of the Hessian's eigenvalues to determine the enhancement. To convert the vessel enhanced data into a vessel segmentation thresholding is required.

Instead of empirical tuning a single global threshold to find a trade-off between small vessel segmentation and noise contamination, multi-class Otsu method (Otsu 1979) and hysteresis thresholding (Fraz et al. 2011) are combined (Mattern 2021a). First, from the vessel enhancement distribution a low and high threshold is determined with a 3-class Otsu approach. The bi-threshold rational is that voxels with enhancement values above the high threshold can be considered vessels and below the low threshold can be considered background with high confidence. For enhancement values in between the thresholds, hysteresis thresholding is leveraged to differentiate between background and vessel. All voxels with enhancement above the high threshold are segmented, while voxels with enhancement between the thresholds are only segmented if they are connected to beforementioned voxels above the high threshold. Therefore, noise contamination is suppressed, while structures with low enhancement, i.e. small vessel, are segmented as long as they are connected to regions with high enhancement, i.e. large vessels. While thresholds were estimated automatically, the following parameters were tuned empirically: Top hat transform with a sphere element with radius 3 and 5 voxels; Frangi filter gamma 0.01 and 0.08, scales [1:1:5] and [1:1:3] voxels for arterial and venous segmentation, respectively.

Computation of vessel distance maps and vessel densities

Vessels inside the putamen were analyzed with conventional vessel densities (i.e. study by Feldman et al. (Feldman et al. 2020)) and VDM (Mattern 2021b; Mattern and Speck 2020; Mattern et al. 2021; Garcia-

Garcia et al. 2023), an approach inspired by recent studies in the field (Huck et al. 2019; Bernier et al. 2018; Bause et al. 2020; Haast et al. 2021; Wei et al. 2022; Mouches and Forkert 2019).

Vessel densities were computed in the native image space, i.e. of the ToF angiography or T2*-weighted data. Per hemisphere a putamen mask (inferred from co-registration to MNI space, see previous section) was used to compute the ratio of detected vessel volume to total putamen volume. Hence, vessel densities summarize the vasculature as the relative volume occupied by segmented vessel.

VDM is based on the vessel segmentation as well and computes for each non-vessel voxel the distance to the closest vessel using the Euclidian distance transform (Maurer et al. 2003). Therefore, VDM provides a distance estimate for each voxel, hence, interpolates the sparse vessel information, which is a distinct difference to region-of-interest (ROI)-wise density estimates (Garcia-Garcia et al. 2023). The VDM source code can be found here: https://github.com/hendrikmattern/VesselDistanceMapping.

Due to the heterogeneous vessel patterns at the mesoscopic scale (i.e. number of arterial stems in the basal ganglia differs across subjects (Akashi et al. 2012; Wei et al. 2022)), no explicit vessel co-registration was performed (i.e. individual vessels were not co-registered with each other). Hence, computing the overlap of vessels on a voxel-bases (i.e. voxel-wise vessel densities) was not performed.

Expert vessel pattern assessment:

To date, the putamen's vasculature is studied in terms of vessels supplying (i.e. the lenticulostriate arteries and the recurrent artery of Heubner (Zunon-Kipré et al. 2012)) and draining the putamen (through small veins originating either from the internal cerebral vein or basal vein (Gillilan 1968)) but not with respect to the vessels' trajectory or pattern. While this origin of supply and drainage is important, we observed that the vessel patterns vary considerably. Hence, the organization of the vessels within the putamen might not be characterized by a single global average, but instead by distinct vessel pattern groups.

This observation was particularly striking when looking at the data on sagittal intensity projections as patterns largely varied in the anterior-posterior direction. Based on these sagittal intensity projections three arterial and four venous patterns were defined empirically for this study (see Figure 2). Although sagittal intensity projects collapse the left-right dimension, hence, the defined patterns are not sensitive to variations along the projection direction, 2D projections render comparison between putamen patterns feasible and easy for human observers. Finding consistent patterns in 3D for the 40 hemispheres included in this study would be non-trivial for humans and is left for machine-based automatic pattern assessment (see next section).

To eliminate any potential bias due to vessel filtering or segmentation, the intensity projections were generated from image data itself after transforming the data to MNI space and applying the putamen masks. For ToF angiography maximum intensity projections (MIP) and for SWI minimum intensity projections (minIP) were used, respectively. Transformation into MNI space improves comparability of patterns further, because the structure was standardized while the vessel organization remained variable (only co-registration of structure, no explicit vessel co-registration).

For the arterial side, three patterns were identified based on the collateralization and span of the fan-like vessel pattern with pattern A having a sparse vasculature and a narrow fan-like pattern, while pattern C

features many collaterals and a fan-like pattern spanning most of the anterior-posterior extent of the putamen. Pattern B has medium collateralization and moderate vessel fanning.

For the venous side, the four patterns were identified based on the vessel sparseness and localization of the vessels itself (propagating through the putamen from inferior or superior direction) with pattern I being very sparse, pattern II having the vasculature localized mainly in the superior part of the putamen, pattern III having the vasculature localized mainly in the inferior part of the putamen, and pattern IV having approximately equal vessels localized in the inferior and superior part of the putamen.

For each arterial and venous pattern, a representative putamen was selected and provided as reference in the expert rating process (representative patterns shown in the top columns and left row of Figure 2). To quantify expert agreement, the mean intraclass correlation coefficient (ICC) was computed for arterial and venous patterns, respectively.

Subsequently, the majority vote for each vessel pattern was computed (20 subjects, 2 hemispheres, arterial and venous side, 80 majority votes in total). These majority votes were used in all subsequent expert assessments.

Automatic vessel pattern assessment and vascular fingerprints

To assess the vasculature in 3D and without requiring expert assignment of the putamen patterns, an automatic vessel pattern pipeline was implemented. To that end, vascular fingerprints were generated. In brief, these fingerprints were generated by transforming the 3D distance maps per putamen into MNI space (spatial normalization), computing the image moments per map, and finding patterns between fingerprints using hierarchical clustering.

Instead of using the distance maps after spatial normalization directly for clustering, using image moments to create a latent space has been proven beneficial (Flusser 2009; Zhang et al. 2015; Hu 1962). In this study central image moments are used which are defined for 3D discretized images $I(x, y, z)$ as (Flusser 2009)

$$\mu_{p,q,r} = \sum_x \sum_y \sum_z (x - \bar{x})^p \, (y - \bar{y})^q \, (z - \bar{z})^r \, I(x, y, z)$$

with $\bar{x}, \bar{y}, \bar{z}$ as the center of gravity and p, q, r as the maximal prescribed order in x, y, and z direction, respectively. In the following, the maximal order is set equally in all three spatial direction and referred to as o. Hence, computing the image moments for a 3D distance map results in a matrix of size $(o + 1, o + 1, o + 1)$, which is subsequently flattened into a 1D vector of length $(o + 1)^3$ (Flusser 2009). To account for the exponential growth of the moment's amplitude with increasing order, the logarithm was computed. While central moments lack rotation and scaling invariance spatial normalization to MNI space prior to computing the moments accounted for the bias explicitly.

By computing the image moments, a 3D distance map was collapsed into a (flattened) 1D vector. This 1D vector then represents the data in a latent space, which we coined vascular fingerprints. Within the latent

space, we approximated the similarity between two individual vascular fingerprints as the Euclidian distance between the corresponding 1D vectors.

To find patterns across vascular fingerprints, hierarchical clustering (Nielsen 2016) with the Ward metric (Ward 1963) was applied. This clustering approach finds patterns by iteratively linking the (groups of) fingerprints which minimize the variance of the clusters being merged. This bottom-up pattern finding was similar to the expert assessment used in this study in which similar pattern pairs were found first and then general descriptions were formulated subsequently.

The outcome of the hierarchical clustering can be represented as a dendrogram (see Figure S1). This tree-like plot represents the linkage between all samples. By defining the number of clusters, from the dendrogram the data is split into distinct pattern clusters (see color coding in Figure S1).

Therefore, the automatic pattern assessment pipeline used in this study had two degrees of freedom: The maximal image moment order o used to compute the vascular fingerprints, ranging from 3 to 33, and the number of clusters to be found, ranging from 2 to 10. To search the parameter space for the optimal clustering parameters the Calinski Harabasz (CH) score (Calinski and Harabasz 1974) was used. This score does not require a ground truth (patterns were found in an unsupervised manner) and is defined as the ratio between the sum of inter-cluster dispersion to the sum of intra-cluster dispersion.

For ToF and SWI clustering the maximal image moment order of $o = 31$ and $o = 33$ were selected, respectively. The number of clusters was chosen to be 7 and 5 for arterial and venous assessment, respectively. The empirical parameter choice was based on the maximal returned CH scores and further explanation on the parameter selection process is provided in the supplementary material (see Figure S2).

Note that the fingerprints and clustering were also computed for the filtered (vessel enhanced) ToF and SWI data respectively, but results with VDM returned higher CH scores (see Figure S2) and, therefore, in the following only the VDM-based clusters are considered.

Quantitative data assessment and statistical comparison

The quantitative assessment was done with two different approaches: First, by computing putamen-wise averaged vessel densities and distances from the data in its respective native image space. Second, by transforming the data into MNI space to look at average distance profiles and voxel-wise comparisons.

Using putamen-wise averaged vessel densities and distances (computed in respective native space) for the arterial and venous vasculature, several assessments were performed. (i) To find significant differences between the left and right hemisphere, the putamen-wise averaged arterial densities, venous densities, arterial distances, and venous distances of all 20 subjects were assessed with paired Wilcoxon signed-rank tests, respectively. The null hypothesis was that the estimates of the left and right hemisphere came for the same underlying distribution. (ii) Pearson correlation between all 40 putamen-wise averaged estimates was used to find significant relations between arterial and venous as well as vessel densities and vessel distances. (iii) Box plots were used to compare differences in putamen-wise averaged estimates between vessel patterns and Mann-Whitney U-rank tests were used to find significant differences between vessel patterns. All statistical test results were Bonferroni-corrected.

To generate the average line profiles along the anterior-posterior (A-P) direction the data was first transformed in to MNI space. Subsequently, for each arterial and venous pattern found by the expert rating and automatic clustering, respectively, the average distance for each voxel along the A-P direction was computed. Hence, the 3D data was summarized into a 1D vector by averaging along 2 dimensions. Further, the 25^{th} and 75^{th} profile were computed.

Further, in MNI-space voxel-wise differences were assessed by subtracting the pattern-wise mean from the global mean per voxel. The degree to which the pattern average deviates from the global mean was reported as relative distance differences in percent. Computing the differences of N patterns to the global mean (yielding N comparisons) was chosen as computing the differences between of all patterns with each other would have resulted in $\binom{N}{2}$ 3D difference image volumes. Hence, the former approach is easier to comprehend, while returning overall lower difference with increasing number of putamen assigned to an individual pattern. Further, this approach measures how much single global mean vessel atlas (i.e. the commonly used vessel mapping approach) and multiple group-specific vessel patterns differ from each other. Note that pattern with only a single putamen assigned (n=1) were omitted from this average distance profile and voxel-wise differences assessment.

Results

For the assessment of the arterial and venous vasculature inside the human putamen at the mesoscopic scale the results are structured in the following order. First, the patterns and their frequencies found by expert and automatic assessment respectively are presented. Subsequently, putamen-wise averaged vessel distances, vessel densities and their correlations are reported including comparisons across vessel patterns. Last, quantitative differences in vessel distances across patterns are assessed using anterior-posterior distance profiles and voxel-wise comparisons.

Expert and automatic pattern assessment

All pattern assessment steps were performed after transforming the data to MNI space. For expert-based pattern assessment sagittal 2D intensity projections were used, while for automatic clustering the 3D VDMs per putamen were leveraged (see methods above). Note, that the expert and automatic pattern assessment represent two different and arguably complementary approaches to finding vessel patterns and not that the automatic pattern pipeline was designed to re-generate the patterns found by experts.

For the expert assessment, the MIPs of the arterial and venous vasculature were grouped empirically and representative example patterns/MIPs were selected (see top row and left column in Figure 2). Subsequently, four raters were provided with the representative patterns and individually assigned a group label per arterial and venous pattern. Inter-rater agreement between experts was high for arterial patterns (ICC3k=0.877, $p < 0.001$) and venous patterns (ICC3k=0.833, $p < 0.001$), respectively. The majority vote per arterial and venous pattern was computed and used in all subsequent analysis.

The occurrence of each arterial-venous pattern combination is shown in Figure 2. Most common arterial pattern was B with 26 out of 40 putamen, accounting for more samples than pattern A and C combined. Hence, most cases have a moderate arterial collateralization and vessel fanning (pattern B). The two most common venous patterns were IV and III with 17 and 12 out of 40 putamen, respectively. Both patterns feature pronounced inferior drainage, hence 72.5% of all cases had prominent drainage via inferior veins.

The arterial and venous pattern combination B-III and B-IV accounted for half of all 40 samples (each pattern combination with 10 putamen, respectively). Subsequently, pattern combination B-I accounts for 5 out of 40 putamen, followed by A-IV (4 putamen) and C-IV (3 putamen). Together these five pattern combinations (i.e. B-III, B-IV, B-I, A-IV, C-III) represent 80.0% of all cases (32 out of 40). Hence, the remaining seven pattern combinations (A-I, A-II, A-III, B-II, C-I, C-II, C-III) account for the remaining 17.5%, each pattern combination with one or two cases, respectively. In general, the venous pattern II was found in only 3 hemispheres, representing the lowest frequency of any arterial or venous pattern

Overall, the expert assessment yields that the putamen vasculature is most commonly characterized by an arterial pattern with moderate collateralization and vessel fanning and veins either with dominant inferior or pronounced inferior and superior drainage.

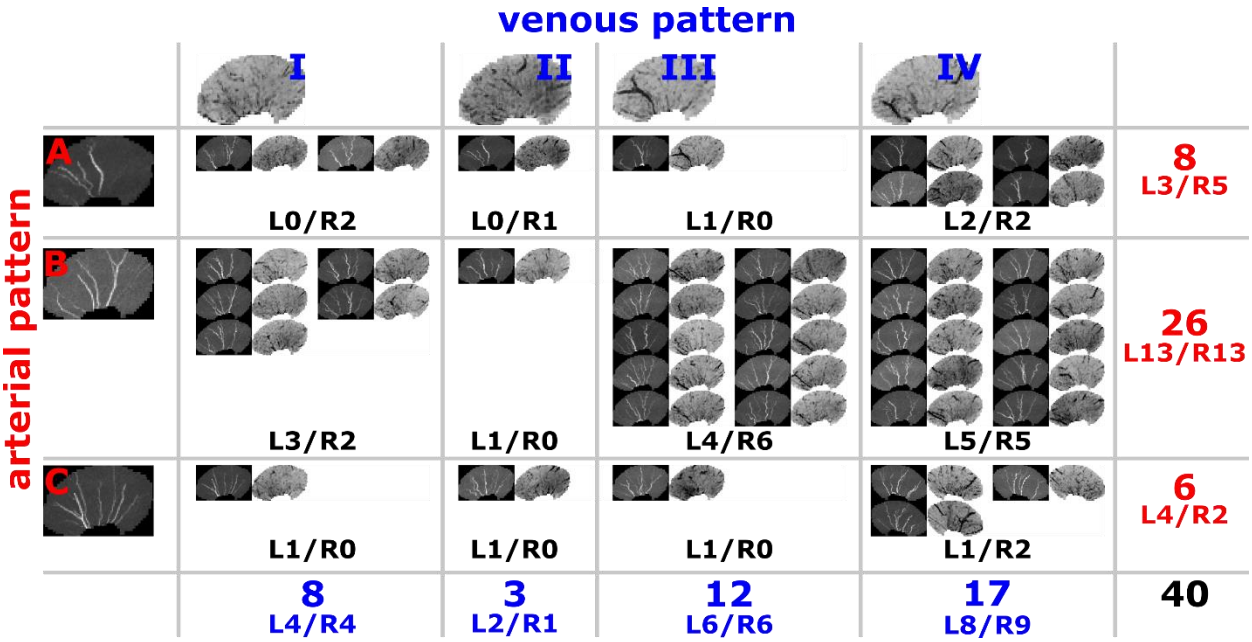

Figure 2: Overview of expert rating on arterial and venous patterns in MNI space. For each hemisphere, the arterial and venous vasculartur is plotted as intentisty projections next to each other. Respresantative MIPs for each pattern are shown in top row/left column and were provided as examples in the expert rating. Global and lateralized pattern frequencies for arterial (red) and venous (blue) pattern are reported, cummulating to 40 hemispheres in total.

For the automatic vessel assessment, patterns were found by hierarchical clustering of the vascular fingerprints for arterial and venous patterns respectively (see Figure S1 for dendrogram). A vascular fingerprint was generated by computing the image moments of the 3D VDM of an individual putamen up to an empirically determined maximal order and flatten the results into a 1D vector. Hence, the fingerprints represent a latent space in which the clustering was performed in an unsupervised manner. Similarity between individual vascular fingerprints was approximated by the Euclidean distance between the respective fingerprints/vectors in the latent space.

In total, seven arterial and five venous patterns were identified. However, three arterial (labeled as “d”, “e”, and “g”) and 2 venous patterns (labeled as “4” and “5”) consisted of a single putamen. For the remaining four arterial and three venous patterns at least 5 putamen were assigned per pattern. Since

this clustering was performed unsupervised, no representative pattern existed ad hoc. Alternatively, group intensity projections were generated. First, MIP and minIP were computed for arterial and venous data, respectively. Then, the samples were pooled by patterns. For each pattern, the corresponding projections were combined into group projection by performing a MIP/minIP once more. The resulting group intensity projections per hemisphere are shown in the top row and left column of Figure 3. Further, Figure 3 shows the frequency of pattern and arterial-venous patterns combinations.

The most frequent arterial patterns were pattern a with 16, c with 10, and f with 6 samples, respectively. While visually pattern f appears more vascularized towards the tail than pattern a, pattern c appears less vascularized than pattern a at the head of putamen. Pattern b appears overall less vascularized than pattern a, c, and f. The most frequent venous patterns were pattern 1 and 3 with 16 samples, respectively, accounting for 80% of all cases. Interestingly, the ratio of left to right putamen was approximately 1:2 and 2:1 for pattern 1 and 3, respectively. Qualitatively, pattern 1 and 3 appear similar, with a slightly more pronounces inferior draining toward the anterior head in pattern 3. Compared to pattern 1 and 3, pattern 2 (6 out of 40 cases) seems overall less vascularized. Further characterization of the automatically determined clustered will be provided in the following sections.

The four most frequent arterial-venous pattern combinations for the automatic clustering were a-3 (9 putamen), a-1 (6 putamen), c-1 (5 putamen) and c-3 (3 putamen), accounting for 57.5% of the 40 samples. The remaining 31 pattern combinations had zero to two samples per pattern. Compared to the expert rating, this sparse pattern combination is driven by the higher number patterns found by the explorative clustering. When neglecting arterial and venous patterns with only one sample, respectively, the combination of visually appearing lower arterial (pattern b, n=5) and lower venous vascularization (pattern 2, n=6), was observed only once (i.e. b-2), while combinations of visually higher arterial and lower venous vascularization and vice versa appeared more frequently, i.e. in total 4 times for pattern b-1 and b-3, and 4 times for pattern a-2, c-2, and f-2

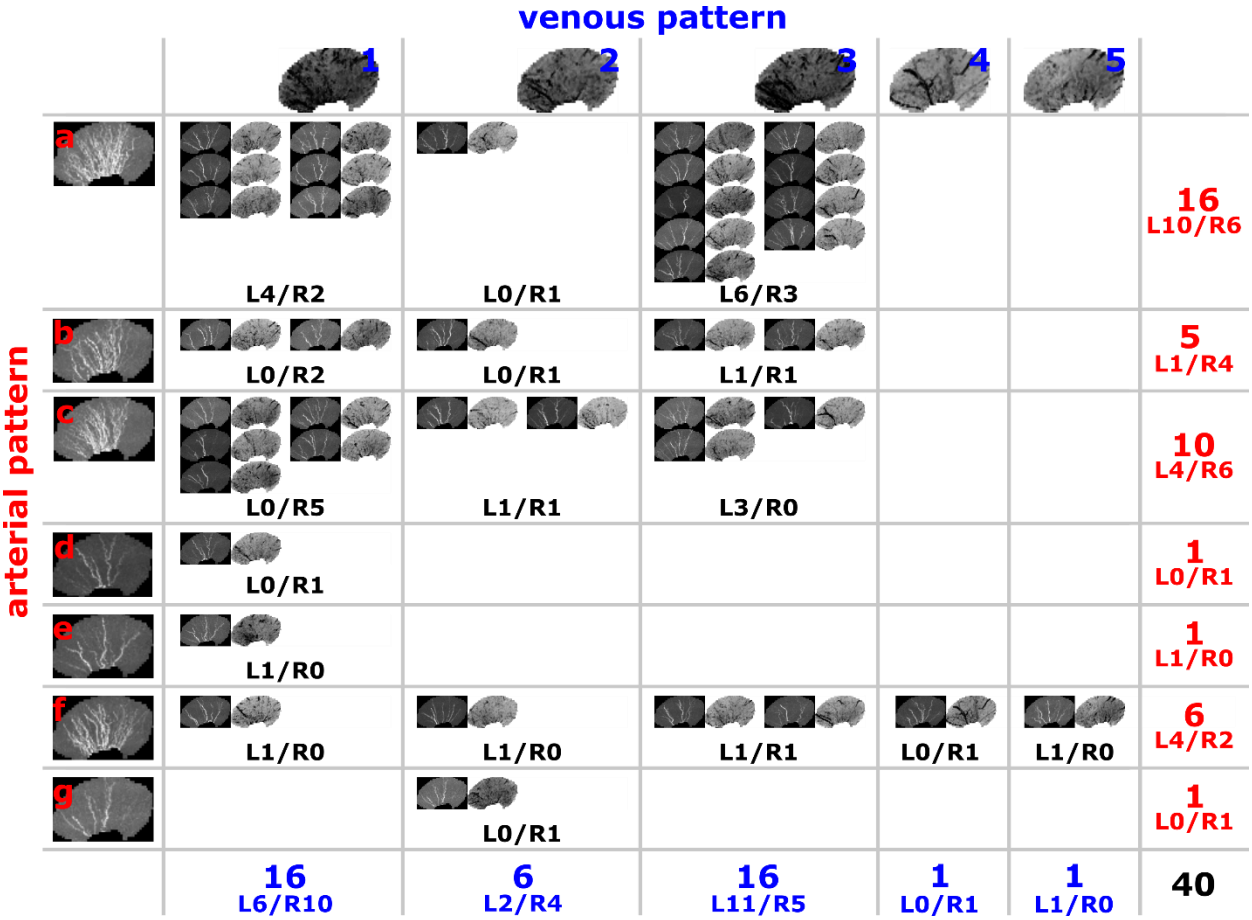

Figure 3: Overview of automatic assessment of arterial and venous patterns in MNI space. For each hemisphere, the arterial and venous vascularture are plotted as intentisty projections next to each other. Group intentisy projections for each pattern are shown in top row/left column. Global and lateralized pattern frequencies for arterial (red) and venous (blue) pattern are reported, cummulating to 40 hemispheres in total.

Assessment of putamen-wise averaged vessel metrics

Summarizing the vasculature into a single number per ROI, i.e. computing the mean vessel density, is common practice. The detailed putamen-wise average vessel estimates are shown in the supplementary material (see Figure S4 and Figure S5 for vessel distances and densities, respectively) and summarized here. For the intra-metric comparison of left and right hemisphere putamen-wise averages, showed significant difference for arterial densities, while all other metrics, i.e. venous densities, arterial distances, venous distances, showed no significant difference. Although densities and distances are conceptional different, i.e. VDM considering the vessel trajectory and densities the pure volume, there was a significant correlation for arterial and venous putamen-wise averages. There was very low, non-significant correlation of arterial vs. venous vessel metrics, i.e. the degree of sparseness in arterial and venous vasculature did not correlate when considering putamen-wise averaged densities and distances. Assessing group differences for patterns found by expert rating and automatic clustering, respectively, returned significant group differences only for putamen-wise averaged venous distances. Beyond significance, visually perceived trends, i.e. sparser vascularization of some patterns, could be observed numerically with the group averages. Nevertheless, putamen-wise averages vessel densities and distances does not

capture fully the differences in spatial vessel trajectories. While these results, indicate the complementary nature of vessel densities and distances, in the following assessments vessel densities are omitted. Given the heterogenous branching patterns of putamen arteries and veins an explicit co-registration of is non-trivial. Hence, vessel distances with their smooth spatial manifestation are used in the following for the projection as well as voxel-wise assessment.

Comparison of group-wise averaged distance profiles

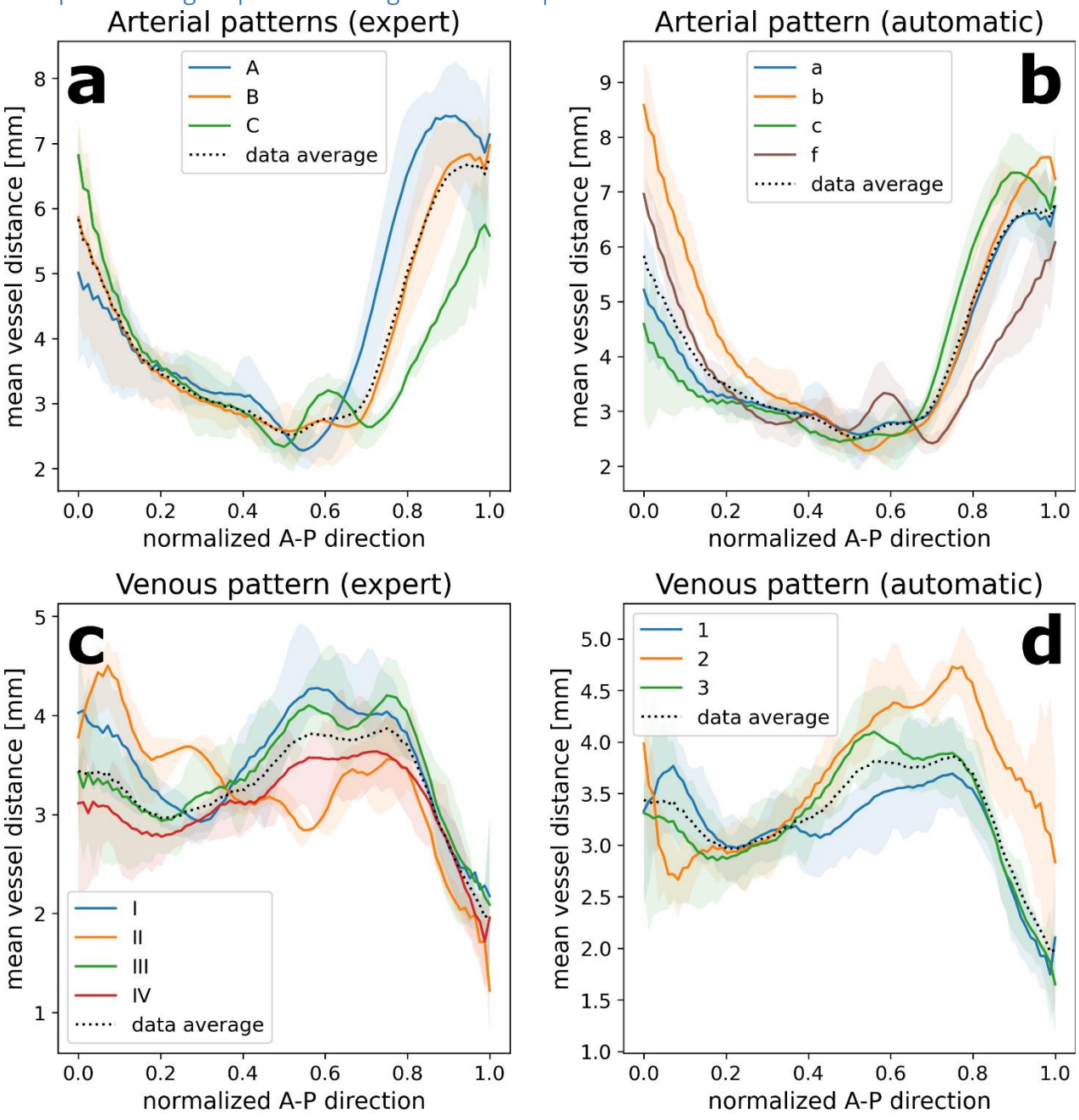

Figure 4: Averaged distance profiles along the anterior-posterior (A-P) direction computed in MNI space. Averaged profiles were obtained for each pattern of the expert and automatic assessment as well as arteries and veins, respectively. Note that patterns

to which only one sample/putamen was assigned were omitted here. Shading around the profiles represents the 25th and 75th percentile of each line profile. Additionally, the global average (computed for all 40 putamen) is plotted as a dotted line (shading for percentiles omitted).

To elucidate the patterns found further, average distance profiles were computed along the anterior-posterior direction after normalization into MNI space (see Figure 4). The anterior-posterior direction was chosen as for arterial patterns, most variance in the vessel patterns was observed in anterior-posterior direction. For the venous patterns, drainage followed either anterior-inferior or posterior-superior prominence, rendering the collapse to 1D feasible. Note that pattern with only a single sample/putamen assigned were omitted, i.e. automatically found patterns d, e, g, 4, and 5.

Overall, the trends observed match with the above qualitative descriptions of patterns and their relations. For the arterial expert ratings, the degree of vascularization, i.e. average distance, increases from pattern A to be to C with the exception of the most anterior part of the putamen where pattern A returns the lowest average vessel distances. For the automatically clustered arterial patterns, above mentioned qualitative trends and average distance profiles are in line as well. Pattern a, c, and f, are similar with higher average distances posterior and lower distances anterior for pattern c compared to pattern a. Comparing pattern f and a, the opposite is true, f is on average more densely vascularized posterior and less anterior than pattern a. Pattern b returns overall larger distances than the other patterns from the anterior to center of the putamen. Interestingly, the pattern C and f, found by expert rating and automatic clustering, respectively, show similar profiles. As expected, pattern B and pattern a, accounting for 65% and 40% of all putamen for the expert rating and automatic clustering, respectively, closely resembles the global mean (computed for all 40 putamen).

In contrast to the arterial pattern, for the expert- and automatic clustering-based venous patterns, no average pattern profile matched the global mean to a large extend. For the expert rating, in the central to posterior part of the putamen pattern I and III and anterior part pattern I and II return the highest average distances. Hence, pattern I and IV showed lowest and highest average vascularization, respectively. For the automatic clustering, pattern 1 and 3 showed similar behavior, with pattern 3 returning higher average distances in the center, and pattern 1 in the anterior head of the putamen. Pattern 2 is distinctively less vascularized in the posterior part of the putamen.

Voxel-wise pattern assessment

To elucidate the spatial patterns in 3D, pattern-wise averaged vessel distance maps are shown in MNI space for 5 representative axial slices along the global mean (computed over all 40 putamen) for expert-based arterial patterns (see Figure 5), clustering-based arterial patterns (see Figure 6), expert-based venous patterns (see Figure 7), and clustering-based venous patterns (see Figure 8), respectively. Note that patterns with only a single putamen are omitted in the figures.

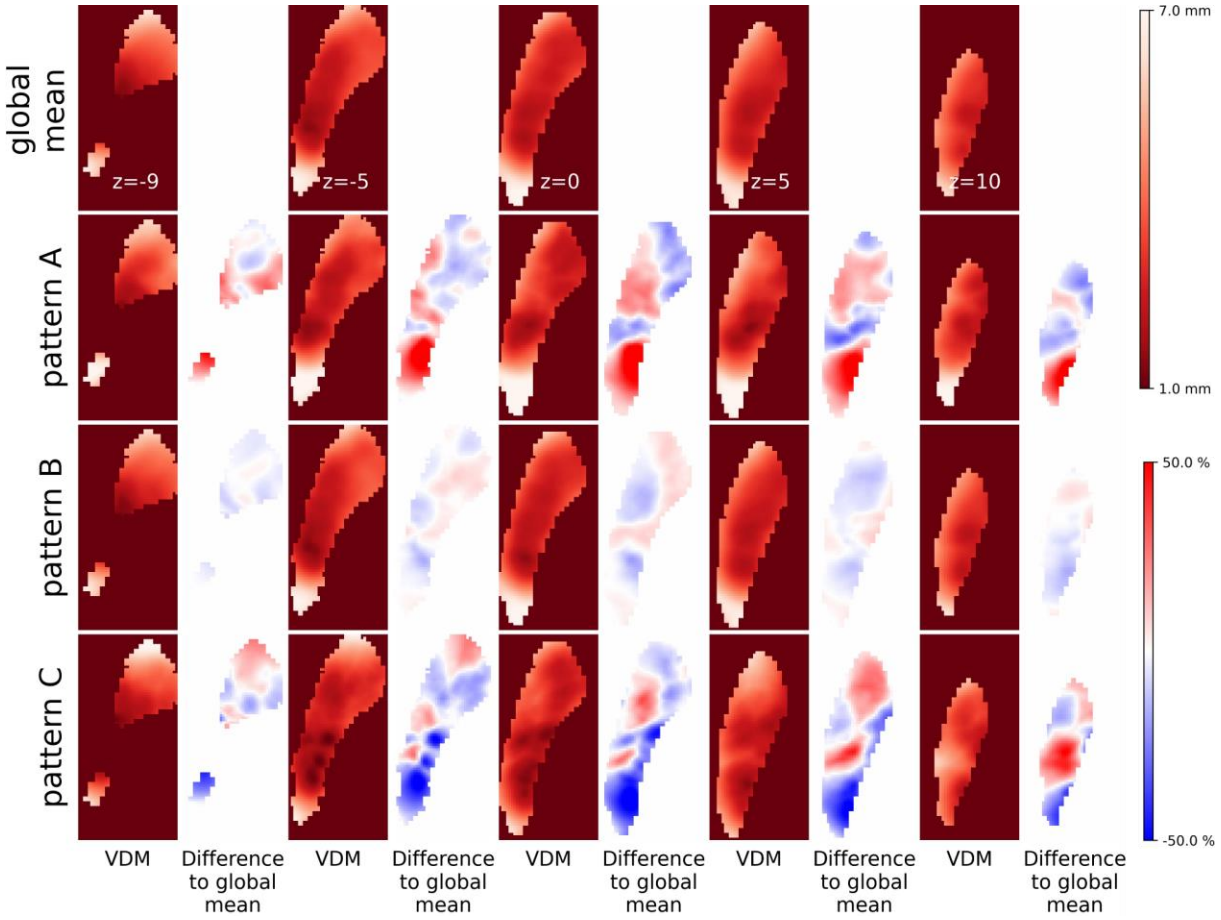

Figure 5: Voxel-wise arterial distances and differences between the global mean (computed for all 40 putamen) and the respective pattern-wise mean found by expert rating. VDMs are shown along the relative distance differences.

For the arterial expert rating, the most frequently assigned pattern B (26 out of 40 putamen) closely resembles the global average (average absolute difference approx. 4%), while pattern A and C show more distinct difference (average absolute difference approx. 15% and 16%, respectively). As prescribed by the empirical pattern definition, pattern A returned an overall higher distance distribution expect for some patches anteriorly. Similarly, pattern C matches the pattern description with markedly lower distance than the global averages at the posterior tails and some patches with higher distance in the central and anterior part of the putamen.

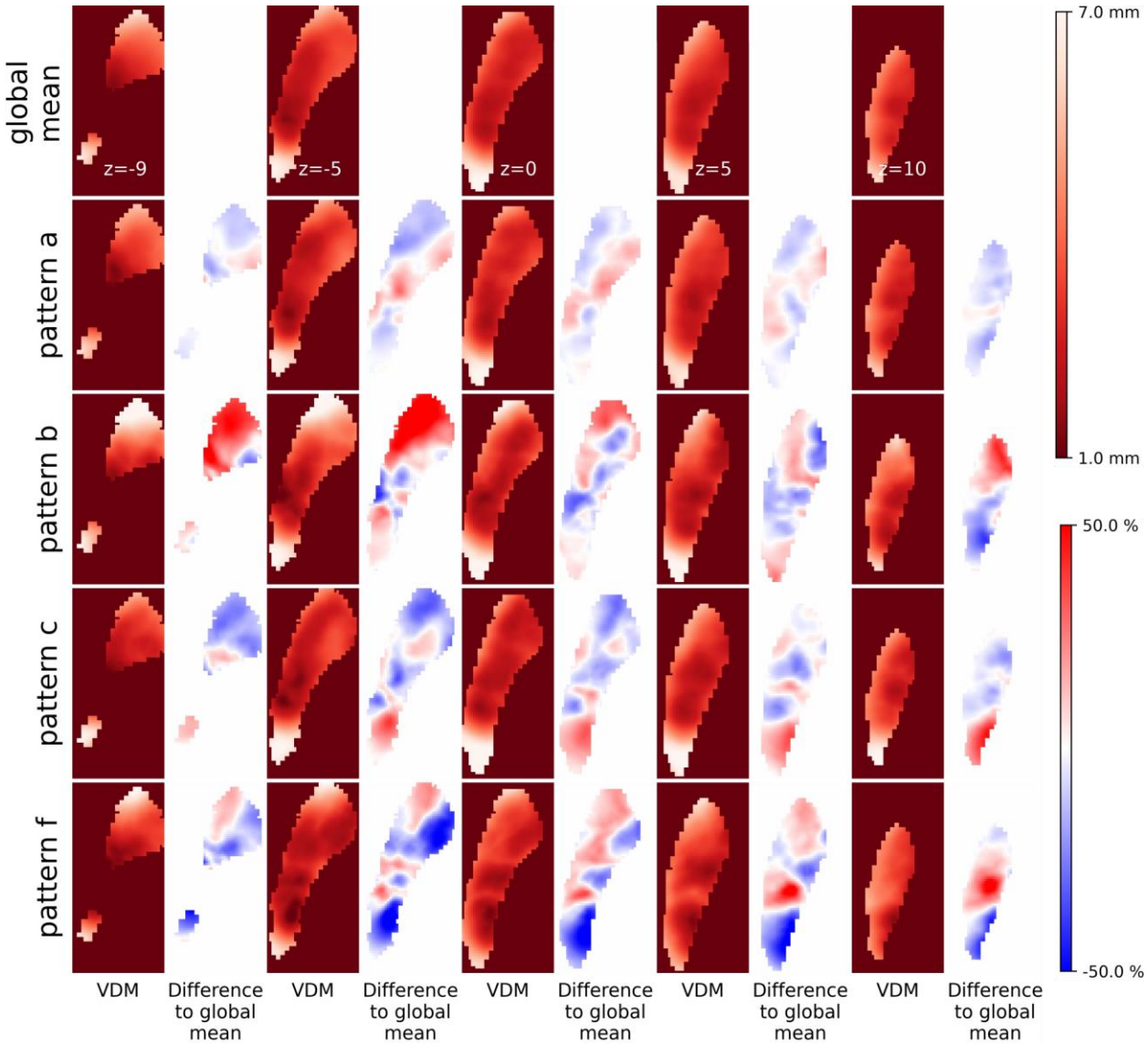

Figure 6: Voxel-wise arterial distances and differences between the global mean (computed for all 40 putamen) and the respective pattern-wise mean found by automatic clustering. VDMs are shown along the relative distance differences. Note that patterns with only a single putamen were omitted.

For the arterial automatic clustering, the most frequently assigned pattern a (16 out of 40 putamen) closely resembles the global average (average absolute difference approx. 7%) while the patterns b, c, and f showed more distinct differences (average absolute difference approx. 16%, 11%, and 17%, respectively). Overall, the 3D pattern distributions observed here matched the trends found with the distance profiles. Overall pattern b returns higher distances anteriorly, patterns c hast higher distances a the most posterior tail of the putamen, and pattern f returns its lowest distances posteriorly.

For both pattern assessments, i.e. expert- and clustering-based, the most frequent patterns closely resemble the global average with additionally patterns representing a gradually increasing or decreasing arterial vasculature in the putamen (i.e. the amount of vessel fanning for expert rating and anteriorly or posteriorly prominent arterial patterns for the automatic clustering).

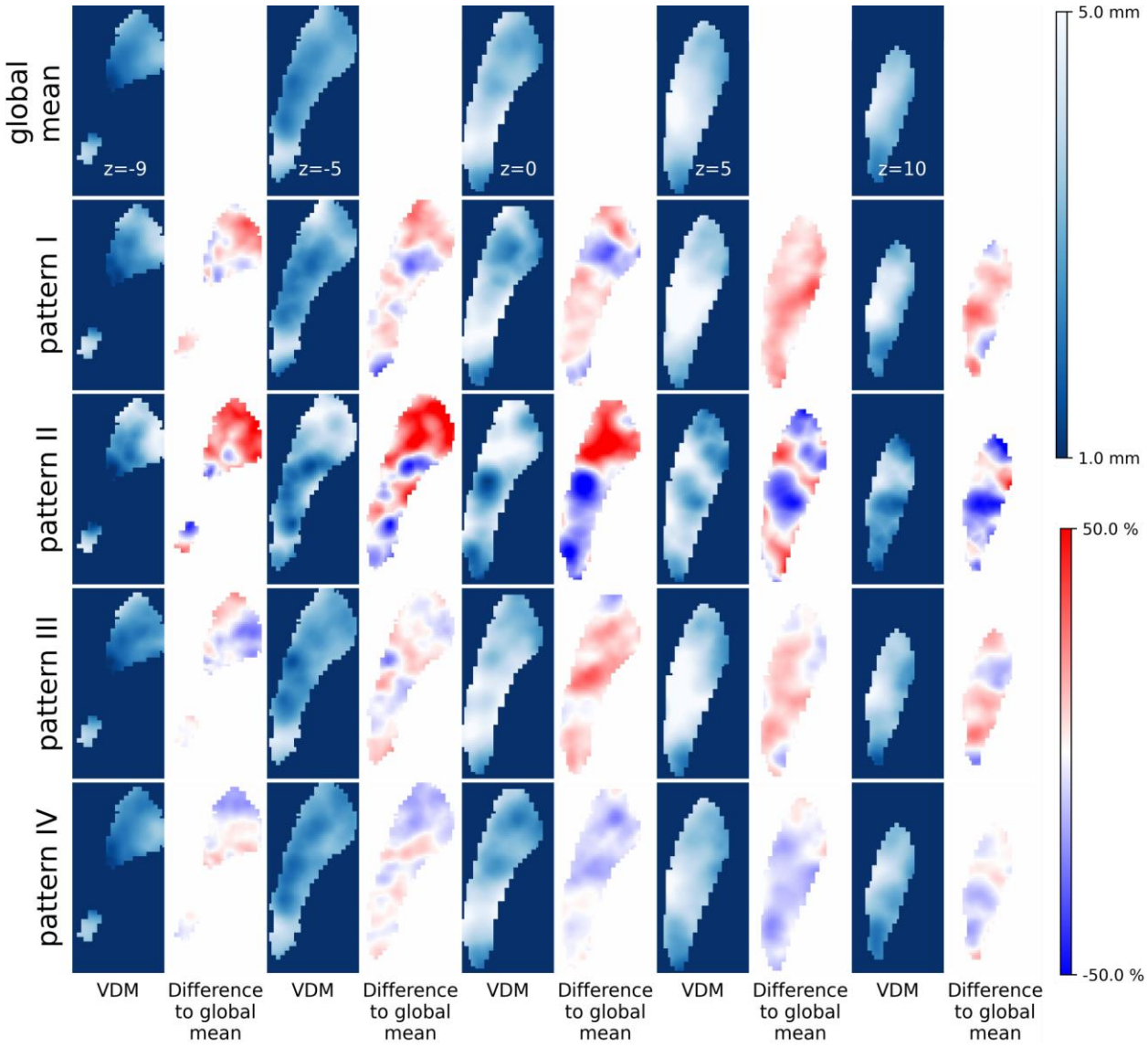

Figure 7: Voxel-wise venous distances and differences between the global mean (computed for all 40 putamen) and the respective pattern-wise mean found by expert rating. VDMs are shown along the relative distance differences.

For the venous expert rating, the least frequently identified pattern II (3 out of 40 putamen) is distinctively different from the global mean (on average an absolute difference of approx. 22%) with higher distances in the anterior part of the putamen and lower distance headwards. This spatial vessel distance distribution matches the empirically derived pattern definition (i.e. pronounced superior drainage). Compared to the global mean, pattern I and III return increasing distances headwards. In contrast, pattern IV showed except for a few small patches and overall lower distance distribution than the global average, indicating the highest vascularization amongst the patterns found. The average absolute differences for pattern I, III, and IV are arguably not distinct (i.e. approx. 10%, 9%, and 7%). Nevertheless, pattern IV (represents 17 out of 40 samples) returned in the comparison here and in the distance profiles overall lower distance than the global average.

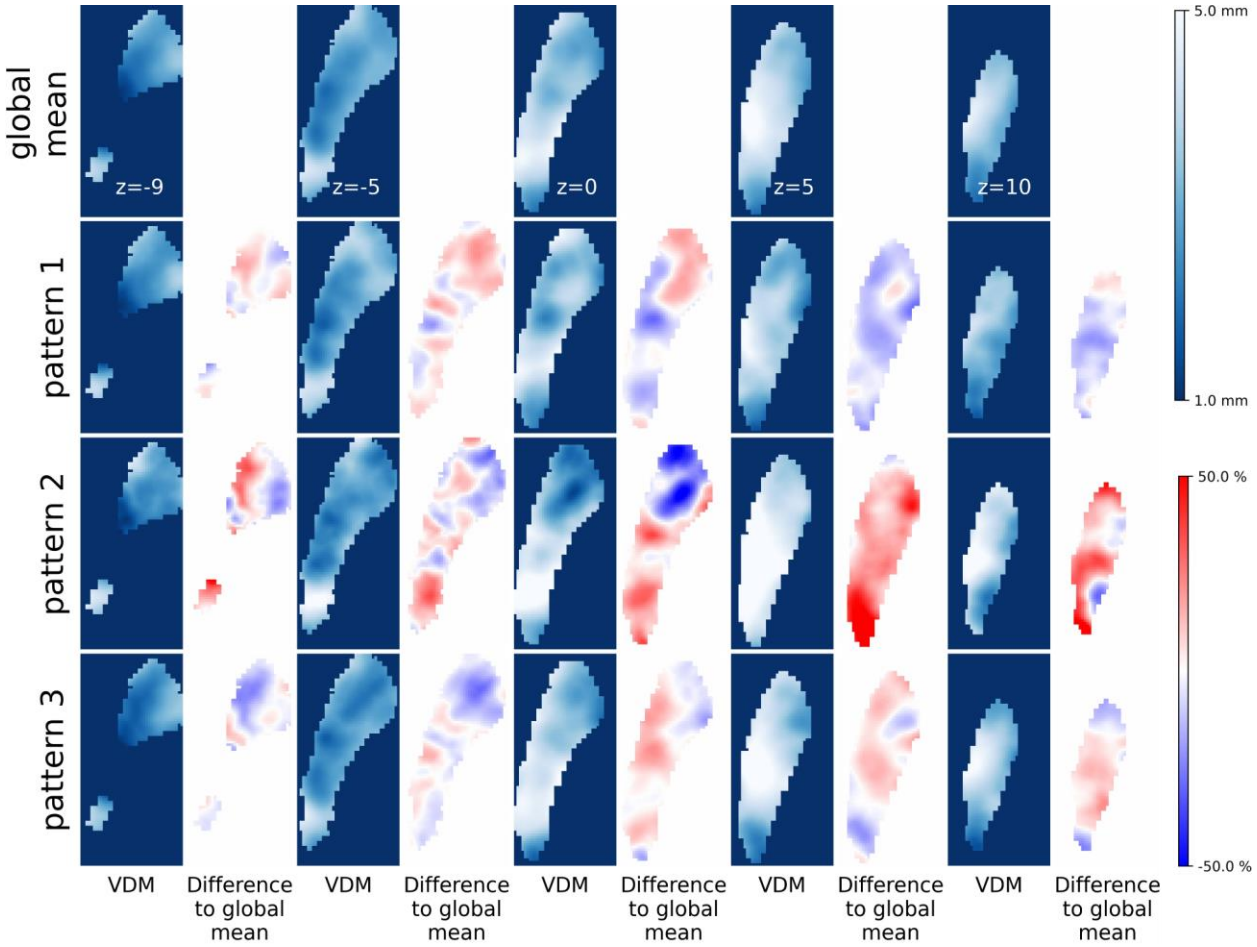

Figure 8: Voxel-wise venous distances and differences between the global mean (computed for all 40 putamen) and the respective pattern-wise mean found by automatic clustering. VDMs are shown along the relative distance differences. Note that patterns with only a single putamen were omitted.

For the venous automatic clustering, pattern 2 is distinctively different from the global mean (on average an absolute difference of approx. 17%) with lower distances in the anterior part of the putamen and higher distance headwards. Pattern 1 and 3 are almost spatially complementary, i.e. if one is below the global mean the other is above (average absolute difference of approx. 8% and 7%, respectively). This is in line with the previous observations as the global mean is largely defined by both pattern, each with 16 out of 40 samples. Hence, the automatic venous clustering suggests that there are at three venous patterns (neglecting single putamen patterns), with two being the most frequent.

For both pattern assessments, i.e. expert- and clustering-based, a single pattern representing the normative vessel trajectory distribution was not found. In contrast, an at least bimodal distance pattern distribution, i.e. with one higher vascularized and one lower vascularized pattern, was more appropriately fitting the data. Hence, these results suggest that the use of a global mean to model the putamen's venous vascularization would be an oversimplification.

Discussion

This study introduced the methodology to assess arterial and venous patterns in the human putamen at the mesoscopic scale with the aim to build a bridge between vascular assessment in neuroscience and

neurology. To that end, VDM was combined with vasculature fingerprints to find arterial and venous vessel patterns respectively via hierarchical clustering. As a complementary approach, expert ratings of empirically defined vessel patterns were obtained for all 40 putamen. Automatic clustering and expert rating found similar distinct vessel patterns in the putamen, with arterial and venous patterns following a unimodal and bimodal distribution, respectively. Beyond the to you best knowledge first description of distinctively different vessel patterns in the human putamen using MRI, this study provides tools to investigate the vasculature beyond global averages, i.e. by identifying vessel patterns in a fully spatially resolved manner.

VDM-based vessel pattern assessment

As a complementary approach to commonly used expert-rating of vessel patterns we leveraged a VDM-based clustering approach. The smooth and continuous nature of VDM omits the need of explicit vessel co-registration, arguably non-trivial at the mesoscopic scale where the vasculature is heterogenous across subjects, i.e. the subject-specific number of vessels. Therefore, only spatial normalization of the structure itself was performed and the structure-vasculature interdependency described by the spatial distribution of vessel distances. Further, as vessel become more spatially specific with decreasing diameter, arguably, the distance of voxel to vessel becomes more relevant, representing an alternative to either pure vessel morphometry (i.e. vessel length, vessel count) and the probability of vessels overlapping across subjects.

To cluster the spatially normalized vessel distance maps the data were first transformed into a latent space via computing the central moments per putamen and flatten the obtained results into a 1D vector, which we coined the vascular fingerprint. Although the hierarchical clustering of these vascular fingerprints was not intended to mimic the expert-based rating, similar patterns can be observed (e.g. arterial pattern C and f) and the same global trends were observed (see next section).

Although improving and standardizing vascular fingerprints and pattern clustering is required in the future, using an automatic approach to assess if distinct vessel patterns exist in an unsupervised manner hold great potential. This is in particular relevant as manual rating are inherently time consuming and challenging with increasing vessel complexity and for larger regions.

Arterial and venous patterns in the putamen

As mentioned above, arterial and venous patterns were observed by the expert rating and automatic clustering. To describe the patterns several approaches were applied, i.e. comparison of 1D distance profiles, 2D intensity projects, and 3D distance maps, all returning coherent results.

In general, arterial vasculature in the putamen follows most frequently a pattern with moderate arterial collateralization and vessel fanning. Patterns deviating from this normative pattern can be observed, but patterns with higher and lower vascularization respectively are observed less frequently.

Overall, the venous patterns in the putamen follow show either a dominant inferior or pronounced inferior and superior drainage. Notably, not a single normative pattern was observed. There are at least two distinct venous patterns in the putamen, one with lower and one with higher vascularization than the global mean. Potential implications of this outcome are discussed in the next section.

When quantifying differences across patterns using putamen-wise averages, the two complementary metrics vessel distances and vessel densities show trends and, in some cases, significant group

differences. Comparing putamen-wise averaged vessel distances and densities in the putamen, no significant correlation between arterial and venous vasculature was observed. Hence, the degree of arterial vascularization does not correlate with the degree of venous vascularization and vice versa. In contrast, Bernier et al. found that arterial and venous densities co-vary. However, this correlation was observed on a whole-brain basis (Bernier et al. 2018). Focusing on a single region such as the putamen in this study could have potentially reduced the value range of (mean) density and distance estimates causing low correlation compared to Bernier et al. (Bernier et al. 2018).

Although these putamen-wise averages results are in line with spatially resolved comparisons, they lack inherently the specificity to show were difference occur. Hence, spatial differences in e.g. the head and tail between patterns can average out. If the variability in the vasculature is mainly along one direction, as the case for the putamen, using 1D average distance line profiles represent an alternative to ROI-wise averages, providing spatial specificity while being easy to comprehend and compare. While increasing the degree of dimensions further, i.e. 2D or 3D, renders comparisons less trivial, certain application will require the additional spatial specificity such as assessing the vessel bias in fMRI. With increasing imaging resolution, correcting vascular biases in functional estimates becomes more relevant (e.g. layer-specific fMRI). Besides physiological aspects of vessel patterns, they can function as vascular resistance and resilience mechanisms in pathologies, rendering vessel mapping and pattern assessment promising tools for the future (Garcia-Garcia et al. 2023; Schreiber et al. 2023; Zhu et al. 2020).

Implications of vessel patterns on vessel mapping and atlases:

In this study we aimed to merge the concepts of vessel patterns with the vessel mapping and atlases. There are two difference scopes of assessing vessel patterns: 1) the dimensionality at which the vasculature is assessed and 2) the degree of vascular variability captured in an atlas or study.

1) ROI-wise summarized vessel metrics can capture changes in vascularization and pathologies-induced group differences, but for a more in-depth analysis they lack spatial specificity. For physiological effects such as the vascular bias in layer-specific fMRI and potential vascular reserves towards pathologies, spatial specificity is key.

2) Computing one vessel atlas across all participants (Huck et al. 2019; Bernier et al. 2018) is a valid approach, especially when dealing with low numbers of samples or if the underlying vasculature is represented by unimodal pattern distribution (i.e. the arterial pattern in this study). However, distinct vessel patterns can exist such as the at least bimodal distribution of venous patterns in this study. For these configurations, a global mean representation can be an oversimplification. Besides the heterogenous vasculature branching and trajectories at the mesoscopic scale studied here, even major cerebral arteries are non-uniform across subjects. Using ToF angiography, for less than 50% of all healthy participants a complete circle of Willis was observed, hence, it is common to observe subject-specific vessel patterns even in larger cerebral arteries (Krabbe-Hartkamp et al. 1998).

Overall, the optimal degree of spatial specificity and number of patterns depend on the study at hand, i.e. number of samples, ROIs included in the analysis, and the variability of the vasculature within ROIs itself. Hence, the concept of vessel patterns and vessel atlases are not mutually exclusive but enrich each other, i.e. by building group-specific vessel atlases (Grabner et al. 2014). Future studies are required to

understand the potential effect of vessel patterns on brain structure and function in health as well as elucidate potential vascular resistance- and resilience-mechanism to pathologies.

Study limitations, strengths and potentials

This explorative, methodology study used part of an openly available data set. Hence, was retrospective in design. Further, only young subjects without any known neurological condition were included and, therefore, all results have to be interpreted in light of the data and cohort at hand. Effects of aging and pathology remain future tasks. Overall, the cohort size was comparable to vessel atlas studies involving 7T imaging, i.e. Huck et al. with 20 subjects (Huck et al. 2019). Nevertheless, the here performed pattern assessment would have benefited from more volunteers.

Further, only the putamen was assessed instead of the more common whole brain analysis (Huck et al. 2019; Ward et al. 2018; Bernier et al. 2018). As part of the basal ganglia, the putamen and its (arterial) vasculature are relevant in several vascular pathologies (Takahashi 2010; Wei et al. 2022) and can be detected reliably using high resolution ToF angiography and susceptibility-based venography (Mattern et al. 2018; Mattern et al. 2019; Akashi et al. 2012; Conijn et al. 2009; Kang et al. 2009; Ward et al. 2018; Huck et al. 2019; Bernier et al. 2018). Further, limiting the scope on one region rendered this proof-of-principle study feasible and extension to the whole brain will be performed in the future.

Imaging resolution and vessel segmentation determine vessel detection and, therefore, represent a considerable bias in vessel distance and density estimates. With higher resolution even smaller vessels would have been depicted and more elaborate segmentation approaches, i.e. (Straub et al. 2022; Chatterjee et al. 2020) would have improved small vessel segmentation further. Note that preliminary results show a linear scaling of vessel distances and densities with the imaging resolution used (Mattern and Speck 2022).

Besides the resolution itself, venous data was acquired at 3T and arterial data at 7T. While the contrast mechanisms of ToF angiography (i.e. inflow enhancement) and SWI (i.e. susceptibility of venous blood) are inherently different, rendering a comparison of their small vessel imaging capabilities non-trivial, there is a confounding factor for the SWI data acquired. A PRESTO sequence was used which did not utilize gradient moment nulling and, therefore, flow artifacts can affect the phase images (Kan et al. 2017). As a result, discontinuities in the venous vasculature were observed in susceptibility maps in this study. Using QSM-based SWI overcomes this challenge in part as it combines the high specificity of the QSM to iron rich-structures and the vessel continuity of the T2*-weighted magnitude images.

No vessel co-registration was performed in this study (only spatial normalization of the brain structure). Previous whole brain vessel atlases used explicit vessel co-registration to achieve overlap of vessel across subjects (Huck et al. 2019; Bernier et al. 2018). Nevertheless, it was reported that with decreasing vessel diameter the vessel patterns become more variable and co-registration more challenging. Arguably, at the mesoscopic scale, the number and orientation of vessels become too variable (Akashi et al. 2012; Wei et al. 2022) to enforce explicit vessel co-registration. Hence, conventional voxel-based vessel densities (i.e. percentage of vessel overlap across subjects) become infeasible but VDM can be used as an alternative when taking the smooth maps and more subtle differences between maps into account.

Conclusion

VDM is a complementary approach to commonly used vessel densities and enables vessel pattern assessment at the mesoscopic scale where co-registration of individual vessels becomes infeasible. Further, the automatic clustering with VDM and vascular fingerprints represents an unsupervised alternative to expert-based pattern assessment. Both pattern assessment, i.e. expert- and clustering-based, found distinct arterial and venous patterns, stimulating the idea of using pattern-specific (vessel) atlases instead of one global average. The here presented methodology could enable future studies to understand the potential effect of the vasculature on brain function in health and disease.

Acknowledgement

The project has been supported by the German Research Foundation (DFG, 9th Nachwuchsakademie Medizintechnik, MA 9235/1-1, and MA 9235/3-1).

The authors declare no conflicts of interest.

Publication bibliography

Acosta-Cabronero, Julio; Milovic, Carlos; Mattern, Hendrik; Tejos, Cristian; Speck, Oliver; Callaghan, Martina F. (2018): A robust multi-scale approach to quantitative susceptibility mapping. In *NeuroImage*. DOI: 10.1016/j.neuroimage.2018.07.065.

Akashi, Toshiaki; Taoka, Toshiaki; Ochi, Tomoko; Miyasaka, Toshiteru; Wada, Takeshi; Sakamoto, Masahiko et al. (2012): Branching pattern of lenticulostriate arteries observed by MR angiography at 3.0 T. In *Japanese journal of radiology* 30 (4), pp. 331–335. DOI: 10.1007/s11604-012-0058-7.

Ashburner, J.; Friston, K. J. (2000): Voxel-based morphometry--the methods. In *NeuroImage* 11 (6 Pt 1), pp. 805–821. DOI: 10.1006/nimg.2000.0582.

Avants, B.; Epstein, C.; Grossman, M.; Gee, J. (2008): Symmetric diffeomorphic image registration with cross-correlation. Evaluating automated labeling of elderly and neurodegenerative brain. In *Medical Image Analysis* 12 (1), pp. 26–41. DOI: 10.1016/j.media.2007.06.004.

Avants, Brian B.; Tustison, Nicholas J.; Wu, Jue; Cook, Philip A.; Gee, James C. (2011): An Open Source Multivariate Framework for n-Tissue Segmentation with Evaluation on Public Data. In *Neuroinform* 9 (4), pp. 381–400. DOI: 10.1007/s12021-011-9109-y.

Bause, Jonas; Polimeni, Jonathan R.; Stelzer, Johannes; In, Myung-Ho; Ehses, Philipp; Kraemer-Fernandez, Pablo et al. (2020): Impact of prospective motion correction, distortion correction methods and large vein bias on the spatial accuracy of cortical laminar fMRI at 9.4 Tesla. In *NeuroImage* 208, p. 116434. DOI: 10.1016/j.neuroimage.2019.116434.

Bernier, Michaël; Cunnane, Stephen C.; Whittingstall, Kevin (2018): The morphology of the human cerebrovascular system. In *Human brain mapping*. DOI: 10.1002/hbm.24337.

Bilgic, Berkin; Xie, Luke; Dibb, Russell; Langkammer, Christian; Mutluay, Aysegul; Ye, Huihui et al. (2016): Rapid multi-orientation quantitative susceptibility mapping. In *NeuroImage* 125, pp. 1131–1141. DOI: 10.1016/j.neuroimage.2015.08.015.

Calinski, T.; Harabasz, J. (1974): A dendrite method for cluster analysis. In *Comm. in Stats. - Theory & Methods* 3 (1), pp. 1–27. DOI: 10.1080/03610927408827101.

Chatterjee, Soumick; Prabhu, Kartik; Pattadkal, Mahantesh; Bortsova, Gerda; Sarasaen, Chompunuch; Dubost, Florian et al. (2020): DS6, Deformation-aware Semi-supervised Learning: Application to Small Vessel Segmentation with Noisy Training Data. Available online at https://arxiv.org/pdf/2006.10802.

Conijn, Mandy M. A.; Hendrikse, Jeroen; Zwanenburg, Jaco J. M.; Takahara, Taro; Geerlings, Mirjam I.; Mali, Willem P. Th M.; Luijten, Peter R. (2009): Perforating arteries originating from the posterior communicating artery: a 7.0-Tesla MRI study. In *European radiology* 19 (12), pp. 2986–2992. DOI: 10.1007/s00330-009-1485-4.

Desikan, Rahul S.; Ségonne, Florent; Fischl, Bruce; Quinn, Brian T.; Dickerson, Bradford C.; Blacker, Deborah et al. (2006): An automated labeling system for subdividing the human cerebral cortex on MRI scans into gyral based regions of interest. In *NeuroImage* 31 (3), pp. 968–980. DOI: 10.1016/j.neuroimage.2006.01.021.

Dufour, A.; Ronse, C.; Baruthio, J.; Tankyevych, O.; Talbot, H.; Passat, N. (2013): Morphology-based cerebrovascular atlas. In : 2013 IEEE 10th International Symposium on Biomedical Imaging (ISBI 2013). San Francisco, California, USA, 7 - 11 April 2013. 2013 IEEE 10th International Symposium on Biomedical Imaging (ISBI 2013). San Francisco, CA, USA, 4/7/2013 - 4/11/2013. Institute of Electrical and Electronics Engineers; IEEE Signal Processing Society; IEEE Engineering in Medicine and Biology Society. Piscataway, NJ: IEEE, pp. 1210–1214.

Feldman, Rebecca Emily; Marcuse, Lara Vanessa; Verma, Gaurav; Brown, Stephanie Sian Gabriella; Rus, Alexandru; Rutland, John Watson et al. (2020): Seven-tesla susceptibility-weighted analysis of hippocampal venous structures: Application to magnetic-resonance-normal focal epilepsy. In *Epilepsia* 61 (2), pp. 287–296. DOI: 10.1111/epi.16433.

Flusser, Jan (2009): Moments and moment invariants in pattern recognition. Chichester, West Sussex, U.K, Hoboken, N.J: J. Wiley.

Forkert, N. D.; Fiehler, J.; Suniaga, S.; Wersching, H.; Knecht, S.; Kemmling, A. (2013): A statistical cerebroarterial atlas derived from 700 MRA datasets. In *Methods of information in medicine* 52 (6), pp. 467–474. DOI: 10.3414/ME13-02-0001.

Frangi, Alejandro F.; Niessen, Wiro J.; Vincken, Koen L.; Viergever, Max A. (1998): Multiscale vessel enhancement filtering. In William M. Wells, Alan Colchester, Scott Delp (Eds.): Medical image computing and computer-assisted intervention. MICCAI'98 : fist international conference, Cambridge, MA, USA, October 11-13,1998 : proceedings, vol. 1496. With assistance of Alan Colchester, Scott Delp, William M. Wells. Berlin: Springer-Verlag (Lecture Notes in Computer Science, 1496), pp. 130–137.

Fraz, M. Moazam; Basit, A.; Remagnino, P.; Hoppe, A.; Barman, S. A. (2011): Retinal vasculature segmentation by morphological curvature, reconstruction and adapted hysteresis thresholding. In : 2011 7th International Conference on Emerging Technologies (ICET 2011). Islamabad, Pakistan, 5 - 6 September 2011. 2011 7th International Conference on Emerging Technologies (ICET). Islamabad, Pakistan, 9/5/2011 - 9/6/2011. International Conference on Emerging Technologies; ICET. Piscataway, NJ: IEEE, pp. 1–6.

Frazier, Jean A.; Chiu, Sufen; Breeze, Janis L.; Makris, Nikos; Lange, Nicholas; Kennedy, David N. et al. (2005): Structural brain magnetic resonance imaging of limbic and thalamic volumes in pediatric bipolar disorder. In *The American journal of psychiatry* 162 (7), pp. 1256–1265. DOI: 10.1176/appi.ajp.162.7.1256.

Garcia-Garcia, Berta; Mattern, Hendrik; Vockert, Niklas; Yakupov, Renat; Schreiber, Frank; Spallazzi, Marco et al. (2023): Vessel distance mapping: A novel methodology for assessing vascular-induced cognitive resilience. In *NeuroImage* 274, p. 120094. DOI: 10.1016/j.neuroimage.2023.120094.

Gillilan, L. A. (1968): The arterial and venous blood supplies to the forebrain (including the internal capsule) of primates. In *Neurology* 18 (7), pp. 653–670. DOI: 10.1212/wnl.18.7.653.

Goldstein, Jill M.; Seidman, Larry J.; Makris, Nikos; Ahern, Todd; O'Brien, Liam M.; Caviness, Verne S. et al. (2007): Hypothalamic abnormalities in schizophrenia: sex effects and genetic vulnerability. In *Biological psychiatry* 61 (8), pp. 935–945. DOI: 10.1016/j.biopsych.2006.06.027.

Grabner, Günther; Dal-Bianco, Assunta; Hametner, Simon; Lassmann, Hans; Trattnig, Siegfried (2014): Group specific vein-atlasing: an application for analyzing the venous system under normal and multiple sclerosis conditions. In *Journal of magnetic resonance imaging : JMRI* 40 (3), pp. 655–661. DOI: 10.1002/jmri.24393.

Haast, Roy A. M.; Kashyap, Sriranga; Yousif, Mohamed D.; Ivanov, Dimo; Poser, Benedikt A.; Khan Ali R (2021): Delineating perfusion and the effects of vascularisation patterns across the hippocampal subfields at 7T. In : Proc. Intl. Soc. Mag. Reson. Med. virtual meeting. ISMRM.

Hanke, Michael; Baumgartner, Florian J.; Ibe, Pierre; Kaule, Falko R.; Pollmann, Stefan; Speck, Oliver et al. (2014): A high-resolution 7-Tesla fMRI dataset from complex natural stimulation with an audio movie. In *Sci. Data* 1 (1), p. 140003. DOI: 10.1038/sdata.2014.3.

Hu, Ming-Kuei (1962): Visual pattern recognition by moment invariants. In *IEEE Trans. Inform. Theory* 8 (2), pp. 179–187. DOI: 10.1109/TIT.1962.1057692.

Huck, Julia; Wanner, Yvonne; Fan, Audrey P.; Jäger, Anna-Thekla; Grahl, Sophia; Schneider, Uta et al. (2019): High resolution atlas of the venous brain vasculature from 7 T quantitative susceptibility maps. In *Brain structure & function*. DOI: 10.1007/s00429-019-01919-4.

Kan, Hirohito; Arai, Nobuyuki; Kasai, Harumasa; Kunitomo, Hiroshi; Hirose, Yasujiro; Shibamoto, Yuta (2017): Quantitative susceptibility mapping using principles of echo shifting with a train of observations sequence on 1.5T MRI. In *Magnetic resonance imaging* 42, pp. 37–42. DOI: 10.1016/j.mri.2017.05.002.

Kang, Chang-Ki; Park, Cheol-Wan; Han, Jae-Yong; Kim, Sang-Hoon; Park, Chan-A; Kim, Kyoung-Nam et al. (2009): Imaging and analysis of lenticulostriate arteries using 7.0-Tesla magnetic resonance angiography. In *Magnetic resonance in medicine* 61 (1), pp. 136–144. DOI: 10.1002/mrm.21786.

Krabbe-Hartkamp, M. J.; van der Grond, J.; Leeuw, F. E. de; Groot, J. C. de; Algra, A.; Hillen, B. et al. (1998): Circle of Willis: morphologic variation on three-dimensional time-of-flight MR angiograms. In *Radiology* 207 (1), pp. 103–111. DOI: 10.1148/radiology.207.1.9530305.

Li, Wei; Wu, Bing; Liu, Chunlei (2011): Quantitative susceptibility mapping of human brain reflects spatial variation in tissue composition. In *NeuroImage* 55 (4), pp. 1645–1656. DOI: 10.1016/j.neuroimage.2010.11.088.

Liu, G.; Sobering, G.; Duyn, J.; Moonen, C. T. (1993): A functional MRI technique combining principles of echo-shifting with a train of observations (PRESTO). In *Magn. Reson. Med* 30 (6), pp. 764–768. DOI: 10.1002/mrm.1910300617.

Makris, Nikos; Goldstein, Jill M.; Kennedy, David; Hodge, Steven M.; Caviness, Verne S.; Faraone, Stephen V. et al. (2006): Decreased volume of left and total anterior insular lobule in schizophrenia. In *Schizophrenia research* 83 (2-3), pp. 155–171. DOI: 10.1016/j.schres.2005.11.020.

Mattern, Hendrik (2021a): Openly available sMall vEsseL sEgmenTaTion pipelinE (OMELETTE). In : Proc. Intl. Soc. Mag. Reson. Med. virtual meeting. ISMRM.

Mattern, Hendrik (2021b): Vessel distance mapping of the aging subcortical venous vasculature. In : ESMRMB 2021, 38th Annual Scientific Meeting, online, October 2 - 7. ESMRMB.

Mattern, Hendrik; Schreiber, Stefanie; Speck, Oliver (2021): Vessel distance mapping for deep gray matter structures. In : Proc. Intl. Soc. Mag. Reson. Med. virtual meeting. ISMRM.

Mattern, Hendrik; Sciarra, Alessandro; Godenschweger, Frank; Stucht, Daniel; Lüsebrink, Falk; Rose, Georg; Speck, Oliver (2018): Prospective motion correction enables highest resolution time-of-flight angiography at 7T. In *Magnetic resonance in medicine* 80 (1), pp. 248–258. DOI: 10.1002/mrm.27033.

Mattern, Hendrik; Sciarra, Alessandro; Lüsebrink, Falk; Acosta-Cabronero, Julio; Speck, Oliver (2019): Prospective motion correction improves high-resolution quantitative susceptibility mapping at 7T. In *Magn. Reson. Med.* 81 (3), pp. 1605–1619. DOI: 10.1002/mrm.27509.

Mattern, Hendrik; Speck, Oliver (2020): Vessel Distance Mapping. In : ESMRMB 2020, 37th Annual Scientific Meeting, online, September 30 - October 2. ESMRMB.

Mattern, Hendrik; Speck, Oliver (2022): Resolution-dependency of arterial and venous density estimates and vessel distance maps in deep gray matter. In : Proc. Intl. Soc. Mag. Reson. Med. London. ISMRM.

Maurer, C. R.; Qi, Rensheng; Raghavan, V. (2003): A linear time algorithm for computing exact Euclidean distance transforms of binary images in arbitrary dimensions. In *IEEE Trans. Pattern Anal. Mach. Intell.* 25 (2), pp. 265–270. DOI: 10.1109/TPAMI.2003.1177156.

Mouches, Pauline; Forkert, Nils D. (2019): A statistical atlas of cerebral arteries generated using multi-center MRA datasets from healthy subjects. In *Sci Data* 6 (1), p. 29. DOI: 10.1038/s41597-019-0034-5.

Nielsen, Frank (2016): Hierarchical Clustering. In : Introduction to HPC with MPI for Data Science: Springer, Cham, pp. 195–211. Available online at https://link.springer.com/chapter/10.1007/978-3-319-21903-5_8.

Otsu, Nobuyuki (1979): A Threshold Selection Method from Gray-Level Histograms. In *IEEE Transactions on Systems, Man, and Cybernetics* 9 (1), pp. 62–66. DOI: 10.1109/TSMC.1979.4310076.

Parker, Dennis L.; Yuan, Chun; Blatter, Duane D. (1991): MR angiography by multiple thin slab 3D acquisition. In *Magn. Reson. Med.* 17 (2), pp. 434–451. DOI: 10.1002/mrm.1910170215.

Perosa, Valentina; Priester, Anastasia; Ziegler, Gabriel; Cardenas-Blanco, Arturo; Dobisch, Laura; Spallazzi, Marco et al. (2020): Hippocampal vascular reserve associated with cognitive performance and hippocampal volume. In *Brain : a journal of neurology*. DOI: 10.1093/brain/awz383.

Schofield, Marvin A.; Zhu, Yimei (2003): Fast phase unwrapping algorithm for interferometric applications. In *Optics letters* 28 (14), pp. 1194–1196. DOI: 10.1364/ol.28.001194.

Schreiber, Stefanie; Bernal, Jose; Arndt, Philipp; Schreiber, Frank; Müller, Patrick; Morton, Lorena et al. (2023): Brain Vascular Health in ALS Is Mediated through Motor Cortex Microvascular Integrity. In *Cells* 12 (6), p. 957. DOI: 10.3390/cells12060957.

Schweser, Ferdinand; Deistung, Andreas; Lehr, Berengar Wendel; Reichenbach, Jurgen Rainer (2011): Quantitative imaging of intrinsic magnetic tissue properties using MRI signal phase: an approach to in vivo brain iron metabolism? In *NeuroImage* 54 (4), pp. 2789–2807. DOI: 10.1016/j.neuroimage.2010.10.070.

Smith, Stephen M. (2002): Fast robust automated brain extraction. In *Human brain mapping* 17 (3), pp. 143–155. DOI: 10.1002/hbm.10062.

Straub, Sina; Stiegeler, Janis; El-Sanosy, Edris; Bendszus, Martin; Ladd, Mark E.; Schneider, Till M. (2022): A novel gradient echo data based vein segmentation algorithm and its application for the detection of regional cerebral differences in venous susceptibility. In *NeuroImage* 250, p. 118931. DOI: 10.1016/j.neuroimage.2022.118931.

Takahashi, Shoki (Ed.) (2010): Neurovascular Imaging. MRI & Microangiography. London: Springer London.

Tustison, Nicholas J.; Avants, Brian B.; Cook, Philip A.; Zheng, Yuanjie; Egan, Alexander; Yushkevich, Paul A.; Gee, James C. (2010): N4ITK: improved N3 bias correction. In *IEEE transactions on medical imaging* 29 (6), pp. 1310–1320. DOI: 10.1109/TMI.2010.2046908.

Viviani, Roberto (2016): A Digital Atlas of Middle to Large Brain Vessels and Their Relation to Cortical and Subcortical Structures. In *Front. Neuroanat.* 10, p. 12. DOI: 10.3389/fnana.2016.00012.

Vockert, Niklas; Perosa, Valentina; Ziegler, Gabriel; Schreiber, Frank; Priester, Anastasia; Spallazzi, Marco et al. (2021): Hippocampal vascularization patterns exert local and distant effects on brain structure

but not vascular pathology in old age. In *Brain Communications*, Article fcab127. DOI: 10.1093/braincomms/fcab127.

Ward, Joe H. (1963): Hierarchical Grouping to Optimize an Objective Function. In *Journal of the American Statistical Association* 58 (301), pp. 236–244. DOI: 10.1080/01621459.1963.10500845.

Ward, Phillip G. D.; Ferris, Nicholas J.; Raniga, Parnesh; Dowe, David L.; Ng, Amanda C. L.; Barnes, David G.; Egan, Gary F. (2018): Combining images and anatomical knowledge to improve automated vein segmentation in MRI. In *NeuroImage* 165, pp. 294–305. DOI: 10.1016/j.neuroimage.2017.10.049.

Wei, Ning; Jing, Jing; Zhuo, Yan; Zhang, Zihao (2022): Morphological characteristics of lenticulostriate arteries in a large age-span population: Results from 7T TOF-MRA. In *Front. Neurol.* 13, Article 944863, p. 1569. DOI: 10.3389/fneur.2022.944863.

Zhang, Yudong; Wang, Shuihua; Sun, Ping; Phillips, Preetha (2015): Pathological brain detection based on wavelet entropy and Hu moment invariants. In *Bio-medical materials and engineering* 26 Suppl 1, S1283-90. DOI: 10.3233/BME-151426.

Zhou, Dong; Liu, Tian; Spincemaille, Pascal; Wang, Yi (2014): Background field removal by solving the Laplacian boundary value problem. In *NMR in biomedicine* 27 (3), pp. 312–319. DOI: 10.1002/nbm.3064.

Zhu, Junxi; Teolis, Spencer; Biassou, Nadia; Tabb, Amy; Jabin, Pierre-Emmanuel; Lavi, Orit (2020): Tracking the adaptation and compensation processes of patients brain arterial network to an evolving glioblastoma. In *IEEE Transactions on Pattern Analysis and Machine Intelligence*, p. 1. DOI: 10.1109/TPAMI.2020.3008379.

Zunon-Kipré, Yvan; Peltier, Johann; Haïdara, Adéréhime; Havet, Eric; Kakou, Médard; Le Gars, Daniel (2012): Microsurgical anatomy of distal medial striate artery (recurrent artery of Heubner). In *Surgical and radiologic anatomy : SRA* 34 (1), pp. 15–20. DOI: 10.1007/s00276-011-0888-5.

Supplementary Material:

Dendrograms for automatic clustering

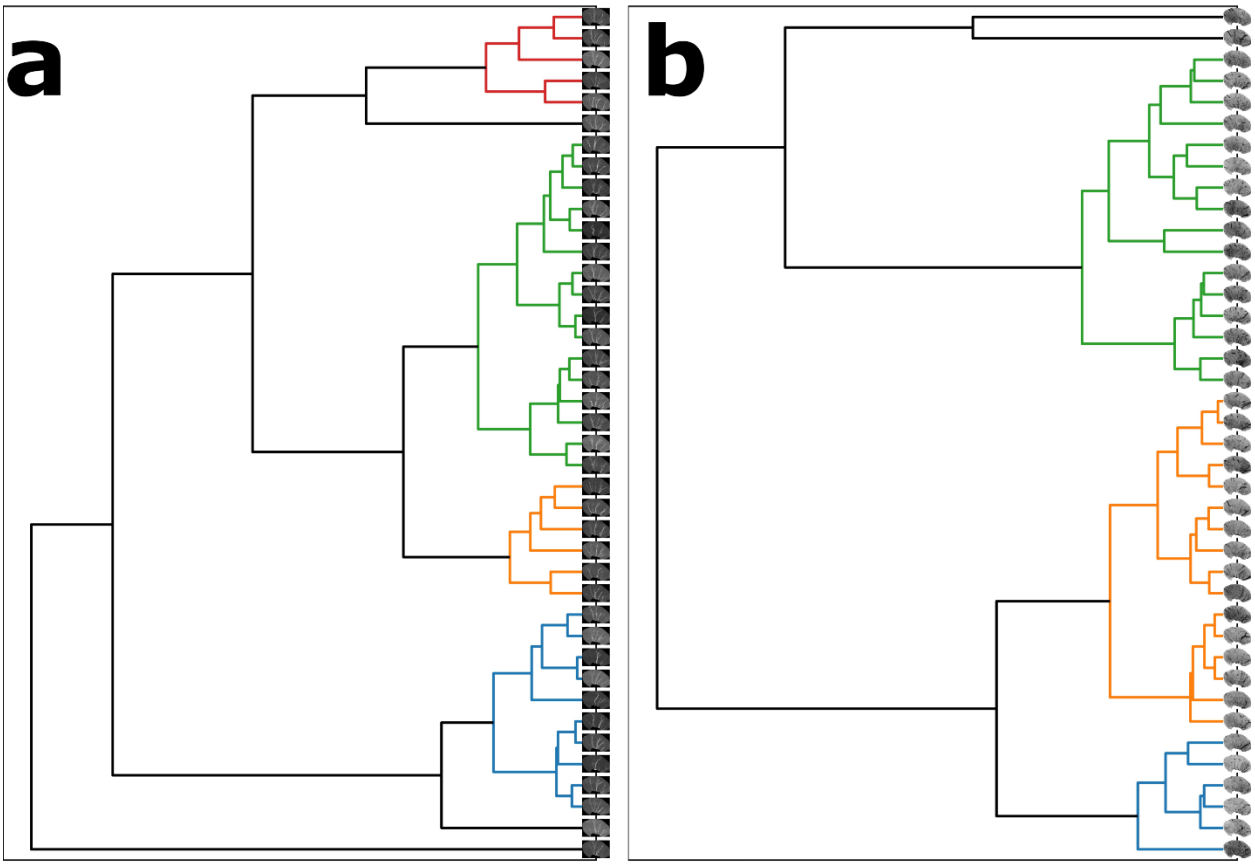

Figure S1: Clustering results represented as dendrograms for the (a) arterial and (b) venous vasculature of the putamen. The patterns where found using VDM data with the parameters returning the highest Calinski-Harabas score. Pattern clusters were color-coded. Note that patterns with only a single putamen were colored black. The x-axis represents the Euclidian distance of the vascular fingerprints (fingerprint introduced as a 1D vector approximating the vasculature's trajectory in a latent space using image moments) and this distance is used to approximate similarity between vessel patterns.

For the clustering for arterial and venous VDM are shown as dendrograms in Figure S1, respectively.

Parameter search for automatic clustering:

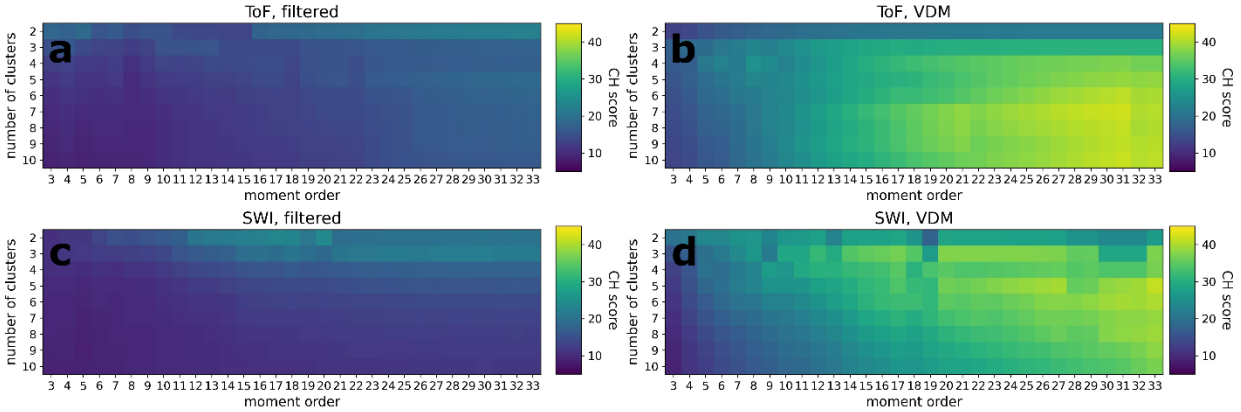

Figure S2: Heatmaps for the Calinski-Harabas (CH) score for the parameter search space for (a, b) arterial (ToF) and (c, d) venous (SWI) data using (a, c) vessel enhanced (filtered) images or (b, d) vessel distance maps (VDM) as inputs for the automatic vessel pattern clustering. The two free variables for the pipeline are the maximal image moment order used to generate the latent space and number of clusters found by the hierarchical clustering approach in the latent space.

The automatic vessel pattern assessment pipeline had two free variables: The maximal order of the image moments o (3 to 33) and the number of clusters (2 to 10). To find the optimal parameter set, the Calinski-Harabasz (CH) score (Calinski and Harabasz 1974) was computed for the parameter space using vessel enhanced (filtered) images and vessel distance maps as inputs, respectively. Overall, VDM-based assessment yielded higher CH scores (see Figure S2), hence, VDM was used for the subsequent pattern analysis.

For ToF VDM data, $o = 31$ and 7 clusters were selected, yielding the highest CH score (42.16) in the selected parameter space.

For SWI VDM data, $o = 33$ and 5 clusters were selected, yielding the highest CH score (41.34) in the selected parameter space.

Correlation of putamen-wise averaged vessel densities and distances

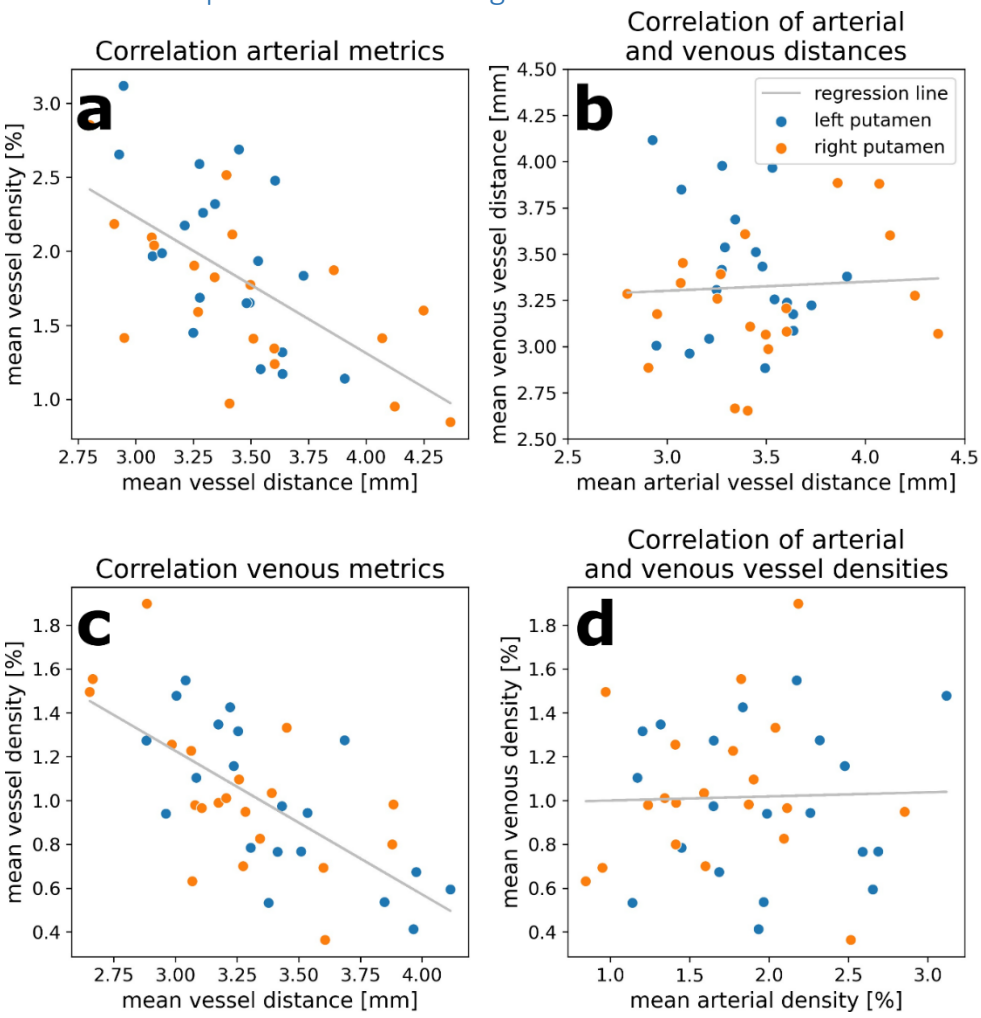

Figure S3: Correlation of vessel densities and distances averaged per putamen for arterial and venous side, respectively. Regression lines are plotted as well as color-coded dots for left and right hemisphere. While the inter-metric comparison shows that mean vessel densities and distances correlate for (a) arterial and (c) venous estimates, respectively, the intra-metric comparison between arterial and venous vasculature showed no significant correlation for either (d) mean vessel densities or (b) distances.

Per putamen, the average vessel density and distance was computed in the respective native image space.

There is a significant correlation of putamen-wise averaged vessel densities and distances for arterial and venous vasculature, respectively ($p<0.0001$ for both; see Figure S3). For arterial estimates, the Pearson regression yields $r=-0.61$, slope=-0.92 %/mm, and an intercept of 5.00 %, while for the venous estimates it yields $r=-0.67$, slope=-0.66 %/mm, and an intercept of 3.19 %.

Correlation of arterial VDM with venous VDM as well as correlation of arterial densities with venous densities were non-significant. Hence, in this study no significant correlation of putamen-wise averaged vessel metrics across the arterial and venous side of the vasculature was detected. Further, the Pearson correlation coefficient was small for VDM ($r=0.05$) and vessel densities ($r=0.03$) across vasculatures (see Figure S3).

When comparing estimates across hemispheres with a paired Wilcoxon signed-rank test, only arterial vessel density estimates returned a significant difference (p=0.014), rejecting the null hypothesis that left and right estimates come from the same underlying distribution. For all other metrics, i.e. venous densities, arterial VDM, and venous VDM, the putamen-wise averages did not differ significantly between left and right hemisphere.

Group differences of putamen-wise averaged vessel densities and distances

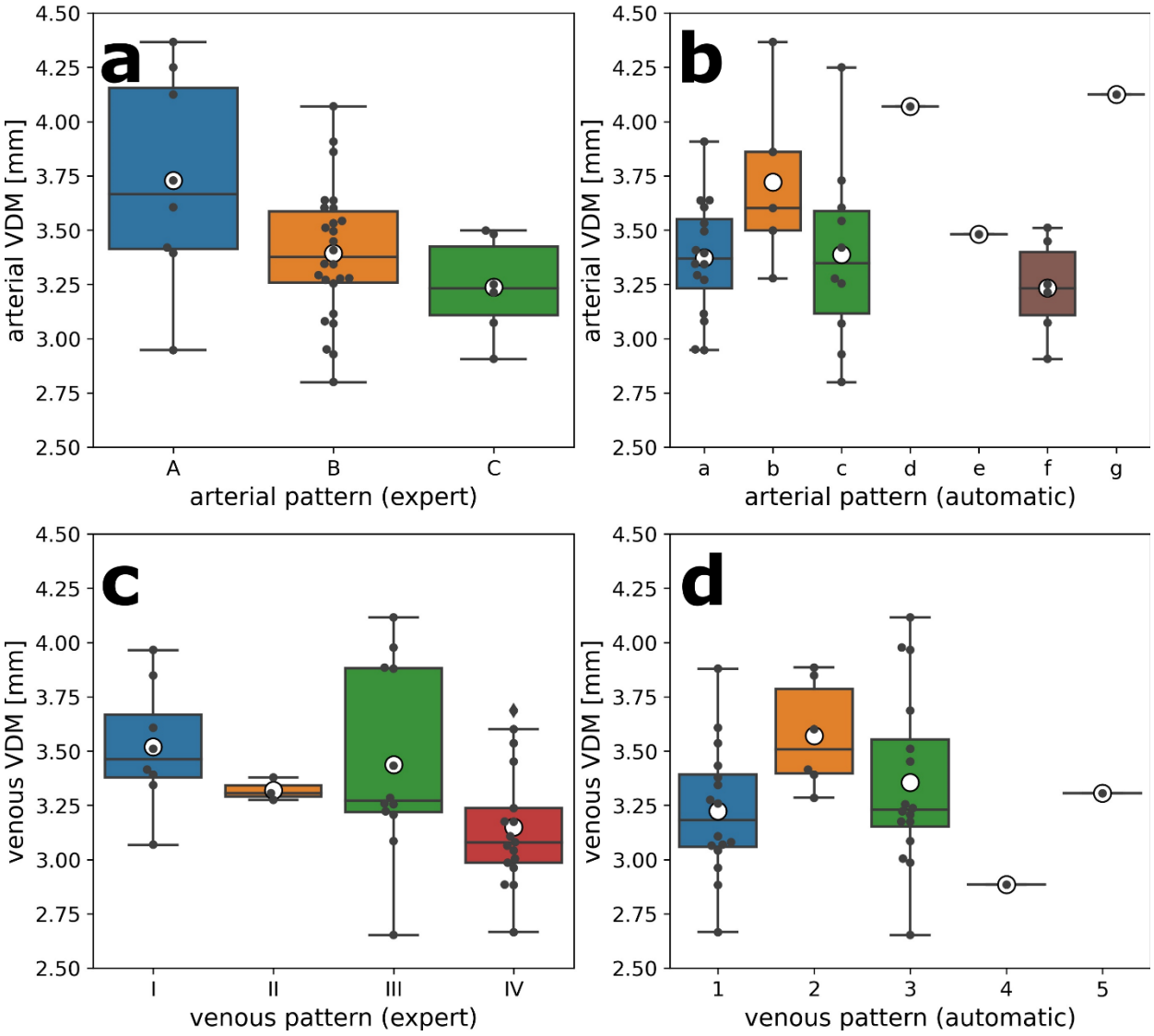

Figure S4: Boxplot of putamen-wise averaged vessel distances grouped by pattern for (a, b) arterial and (c, d) venous vasculature, respectively. Patterns are based on the (a, c) expert rating and (b, d) automatic clustering. Group mean is indicated by the white dot, median by the black horizontal line, quartiles by the extent of the box, and the whiskers extending to 1.5 times the interquartile range below/above the low/high quartiles (values outside whiskers considered as outliers). Additionally, each data point is scatter plotted. No significant group difference was found.

Per putamen, the average vessel density and distance was computed in the respective native image space. Subsequently, Mann-Whitney U-rank tests were applied to find significant differences between pattern-

wise distribution of average vessel metrics (see Figure S4 and Figure S5 for vessel distances and densities, respectively). Significant differences after correction for multiple comparisons was found only for venous vessel distances and patterns based on expert rating, i.e. pattern I vs. IV ($p<0.001$), and pattern II vs. IV ($p<0.05$). Beyond significant differences, trends were observed with overall larger group differences for vessel densities than for distances.

Since the arterial expert rating differentiated patterns based on the arterial collateralization and vessel fanning, the decrease of arterial distances from pattern A to C was expected (approx. -13% and -12% for mean and median, respectively). However, arterial density did not show the expected increase. Hence, mean arterial VDM values mimic the perceived pattern better then mean arterial densities. Similarly, expert rating of venous patterns was based on the vessel sparseness and localization of the vessels itself. Therefore, a decrease in venous distances and an increase in density from pattern I to IV was expected (approx. -11%/-12% for mean/median distances, and +84% /+80% for mean/median densities, respectively). Further, a monotonic increase in mean and median venous densities as well as decrease in median distances was observed from pattern I to IV.

The automatic pattern assessment was unsupervised. Hence, comparing pattern-wise mean/median estimates is not a validation of the patterns found, but rather an explorative assessment. Note that some of the patterns found consisted of a single putamen (pattern with n=1). For the arterial patterns, putamen-wise averaged density and distance estimates show similar behavior for pattern a, c, and f. Pattern b is on average less vascularized than pattern a, c, and f (approx. -9%/23% for b vs. a, approx. -10%/34% for b vs. c, and approx. -13%/32% for b vs. f, in mean distances and densities, respectively). For the patterns with n=1, d and g had an overall low vascularization while pattern e appeared similar to the patterns a, c, and f, requiring an assessment beyond putamen-wise averages to disentangle difference. For the automatic clustering of the veins, pattern 2 is on average less vascularized than pattern 1 and 3 (approx. -10%/16% for 2 vs. 1, approx. -6%/33% for 2 vs. 3 in mean distances and densities, respectively). Pattern 1 and 3 have similar median values, but have differences in mean due to the larger data spread of pattern 3. For patterns with n=1, 4 appears highly vascularized, returning the highest venous density of all putamen, while pattern 5 appears comparable to pattern 1, 2, and 3.

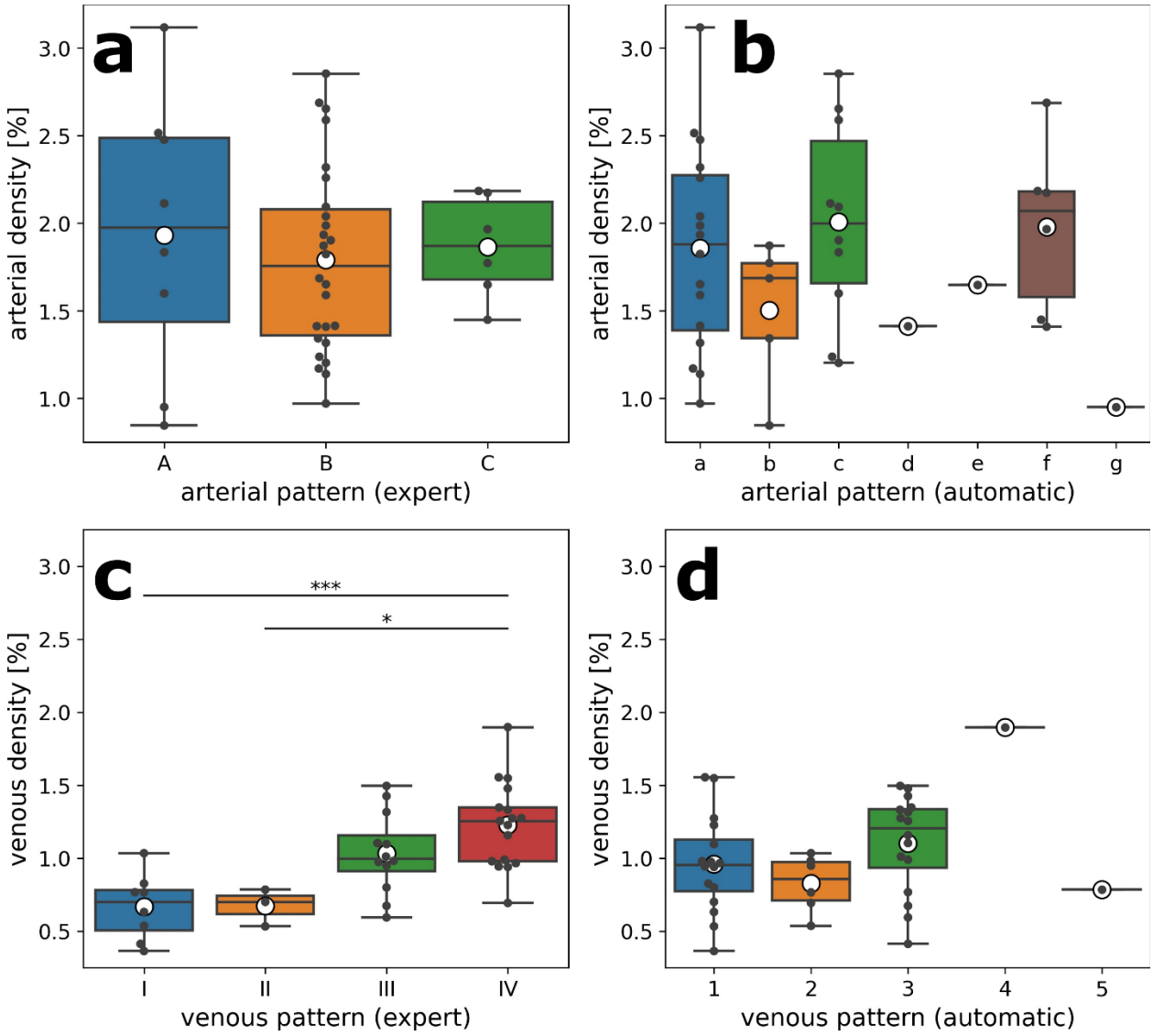

*Figure S5: Boxplot of putamen-wise averaged vessel densities grouped by pattern for (a, b) arterial and (c, d) venous vasculature, respectively. Patterns are based on the (a, c) expert rating and (b, d) automatic clustering. Group mean is indicated by the white dot, median by the black horizontal line, quartiles by the extent of the box, and the whiskers extending to 1.5 times the interquartile range below/above the low/high quartiles (values outside whiskers considered as outliers). Additionally, each data point is scatter plotted. Significant group difference (Bonferroni-corrected) was found for venous expert-based patterns I vs. IV ($p<0.001$***) and II vs. IV ($p<0.05$*)*

The statistics per pattern of the putamen-wise averaged vessel distances and densities are shown as numerical values in the tables Table S1, Table S2, Table S3, and Table S4, respectively.

Table S1: Putamen-wise averaged arterial vessel densities and distances reported per group/pattern as mean ± standard deviation, median using patterns found by the expert assessment

	Pattern A	Pattern B	Pattern C
Mean arterial distance [mm]	3.729 ± 0.457; 3.667	3.394 ± 0.300; 3.376	3.237 ± 0.210; 3.231
Mean arterial density [%]	1.931 ±- 0.736; 1.974	1.790 ± 0.523; 1.755	1.866 ± 0.269; 1.869

Table S2: Putamen-wise averaged arterial vessel densities and distances reported per group/pattern as mean ± standard deviation, median using patterns found by the automatic pipeline

	Pattern a	Pattern b	Pattern c	Pattern d	Pattern e	Pattern f	Pattern g
Mean arterial distance [mm]	3.372 ± 0.256; 3.369	3.721 ± 0.373; 3.601	3.387 ± 0.402; 3.348	4.070 ± 0.000; 4.070	3.481 ± 0.000; 3.481	3.234 ± 0.207; 3.231	4.125 ± 0.000; 4.125
Mean arertial density [%]	1.858 ± 0.571; 1.879	1.503 ± 0.374; 1.686	2.008 ± 0.542; 1.998	1.412 ± 0.000; 1.412	1.649 ± 0.000; 1.649	1.978 ± 0.445; 2.070	0.950 ± 0.000; 0.950

Table S3: Putamen-wise averaged venous vessel densities and distances reported per group/pattern as mean ± standard deviation, median using patterns found by the expert assessment

	Pattern I	Pattern II	Pattern III	Pattern IV
Mean venous distance [mm]	3.519 ± 0.268; 3.462	3.320 ± 0.043; 3.306	3.438 ± 0.416; 3.271	3.149 ± 0.269; 3.080
Mean venous density [%]	0.667 ± 0.210; 0.698	0.672 ± 0.104; 0.700	1.035 ± 0.266; 0.996	1.226 ± 0.286; 1.255

Table S4: Putamen-wise averaged venous vessel densities and distances reported per group/pattern as mean ± standard deviation, median using patterns found by the automatic pipeline

	Pattern 1	Pattern 2	Pattern 3	Pattern 4	Pattern 5
Mean venous distance [mm]	3.224 ± 0.293; 3.183	3.571 ± 0.229; 3.508	3.356 ± 0.390; 3.230	2.885 ± 0.000; 2.885	3.306 ± 0.000; 3.306
Mean venous density [%]	0.959 ± 0.321; 0.954	0.826 ± 0.177; 0.857	1.102 ± 0.323; 1.206	1.898 ± 0.000; 1.898	0.784 ± 0.000; 0.784